Università degli Studi di Palermo

FACOLTÀ DI INGEGNERIA

Dipartimento di Energia, ingegneria dell'Informazione e modelli Matematici (DEIM)

Dottorato in Ingegneria Elettronica e delle Telecomunicazioni

- XXIV Ciclo -

Settore Scientifico-Disciplinare: ING-INF/01

TESI DI DOTTORATO

THE SILICON PHOTOMULTIPLIER: AN IN-DEPTH ANALYSIS IN THE CONTINUOUS WAVE REGIME

Candidato

Ing. Gabriele Adamo

Tutor

Ch.mo Prof. Alessandro Busacca

Coordinatore

Ch.mo Prof. Giovanni Garbo

Triennio 2011 - 2013

DOTTORATO

"If everything seems under control, you're not going fast enough."

Mario Andretti

UNIVERSITY OF PALERMO

Abstract

PhD Course in Electronics and Telecommunications Engineering
Department of Energy, Information engineering and Mathematical models (DEIM)

Doctor of Philosophy

The Silicon Photomultiplier: An In-Depth Analysis In The Continuous Wave Regime

by Gabriele Adamo

The Silicon Photomultiplier (SiPM) is a novel solid state photon counting detector consisting of a parallel array of avalanche photodiodes biased beyond their breakdown voltage. It has known a fast development in the last few years as a possible alternative to vacuum photomultiplier tubes (PMTs) and conventional avalanche photodiodes (APDs). Indeed, current research in photodetectors is directed toward an increasing miniaturization of the pixel size, thus both improving the spatial resolution and reducing the device dimensions. SiPMs show high photon detection efficiency in the visible and near infrared range, low power consumption, high gain, ruggedness, compact size, excellent single-photon response, fast rise time and reduced sensitivity with temperature, voltage fluctuations, and magnetic fields. Furthermore, solid-state technology owns the typical advantages of the planar integration process, therefore, they can be manufactured at low costs and with high reproducibility.

SiPMs performances in photon counting regime have been deeply investigated in literature, using picosecond pulsed lasers. In this regime, they can be used in applications like positron emission tomography, magnetic resonance imaging, nuclear physics instrumentation, high energy physics. An optical characterization performed via continuous wave (CW) sources has seldom been reported even though this kind of excitation seems to be very useful in several fields such as low power measurements, near-infrared spectroscopy and immunoassay tests.

In this Thesis, I perform an electrical and optical analysis of two novel classes of SiPMs in the CW regime. After a brief introduction about the SiPM operating principle, parameters and properties (**Chapter 1**), I describe my responsivity measurements made with an incident optical power down to tenths of picowatts, monitoring the temperature of the device packages, and on a spectrum ranging from ultraviolet to near infrared (**Chapter 2**). These measurements allowed to define an innovative criterion to establish the conditions necessary for the device to be usable in CW regime.

Chapter 3 continues with an investigation of the SiPM signal-to-noise ratio. Measurements employed a 10 Hz equivalent noise bandwidth, around a tunable reference frequency in the range 1 - 100 kHz, and were performed varying the applied bias and the temperature of the SiPM package. These results were compared with similar measurements performed on a PMT.

Once the SiPM is characterized, **Chapter 4** reports an innovative application: an optical characterization of a class of photonic crystals infiltrated with a new ethanol responsive hydrogel employing the SiPM as a reference photodetector. This activity shows innovative developments for the ethanol sensing to be applied into inexpensive and minimally invasive breathalyzers.

Finally, **Appendix A** shows an electro-optical characterization of a novel class of Silicon Carbide (SiC) vertical Schottky UV detectors. I performed responsivity measurements as a function of the wavelength and the applied bias, varying the temperature of the SiC package, in the 200 - 400 nm range.

The results of this work show a new approach to investigate the SiPM capabilities, the CW regime, demonstrating its outstanding performances and innovative applications.

This Thesis was made in collaboration with the "Advanced Sensors Development Group" of STMicroelectronics and partially supported by the Project HIGH PROFILE (HIGH-throughput PROduction of FunctIonaL 3D imagEs of the brain), which is funded by the European Community under the ARTEMIS Joint Undertaking scheme.

Acknowledgements

This research work would not have been possible without the support of the Laboratory of Optics and OptoelectroniX (LOOX) research group. First, I would like to express my deep gratitude to my tutor Professor Dr. Alessandro C. Busacca, which provided me not only insightful guidelines and suggestions, but also the enthusiasm and the method for the research work. Thanks for believing in me and my work, thanks for your scientific guidance, for your valuable comments on the experimental results and for your advice. I enjoy working with him and with the whole group at the University of Palermo. This group exists thanks to his precious support. I will never forget what he did and he is still doing for me.

Deep gratitude is also due to Prof. Dr. Stefano Riva Sanseverino who, together with Prof. Busacca, gave me the opportunity to begin my PhD and helped me to define my scientific research path.

A big thanks goes to my colleagues and friends Dr. Salvatore Stivala and Dr. Antonino Parisi that provided their invaluable expertise during experiments, sharing with me the long hours spent in front of the monochromator, and during the draft of the papers. I learned a lot from their great determination, effectiveness, knowledge, assistance and their teachings and they made me able to work independently.

I enjoyed working with Dr. Luciano Curcio and I am grateful to him for his friendship and enjoyable technical discussions. My gratitude goes to all the LOOX members, not only for their scientific support, but also for their friendship: Andrea Andò, Diego Agrò, Riccardo Pernice, Alessandro Tomasino, Giuseppe Morsellino, Maurizio Pinto, Riccardo Canicattì, Vincenzo Rocca. Thanks to all these people I never felt alone and I enjoyed a lot these three years.

Finally, I want to thank my family that always accepted and supported my choices, always giving me sincere advice.

Contents

List of Figures

Chapter 1

The Silicon Photomultiplier: an Unlimited Device for Future Applications

1.1 The origins

The detection of very low intensity levels of light became possible almost one century ago when in the year 1913 Elster and Geiter invented the photoelectric tube. Only few years later Einstein formulated the photoelectric workfunction (publishing a paper that explained the photoelectric effect as being the result of light energy carried in discrete quantized packets) [1].

More than 20 years passed until the first photomultiplier tube (PMT) was invented and became a commercial product in 1936. Single photons were detectable from now on. Further innovations have led to highly sophisticated devices available nowadays. PMTs have different strong handicaps: they are very sensitive to magnetic fields, their operating biases are high (hundreds of Volts), they are fragile with regard to mechanical stress and input surges, they are not properly compact and their price is high because the complicated mechanical structure inside the vacuum container is mostly handmade [2, 3]. This forced research toward the finding of an alternative to PMTs [4].

The PIN photodiode was a good candidate, being used in high-energy physics. The acronym PIN describes the structure and stands for p-doped silicon, intrinsic and n-doped. Even with a state of the art charge sensitive amplifier, which is needed because the device has no internal gain, the noise is at the level of several hundred electrons and

consequently the smallest detectable light flash needs to consist of even more photons [5].

Avalanche photodiodes (APDs), instead, show an internal gain which improves the signal-to-noise ratio, with respect to PIN, but still around 20 photons are needed for a detectable light pulse. The excess noise factor, being connected to the fluctuation of the avalanche multiplication, limits the useful range of the gain [3].

At the beginning of current millennium the Geiger mode Avalanche PhotoDiode (G-APD), also called Single-Photon Avalanche Diode (SPAD), has been developed. This paved the way to the realization of the Silicon PhotoMultiplier (SiPM): a structure based on a planar pixel array of SPADs capable of detecting single photons like a PMT [2, 3].

1.2 The SPAD

A SPAD is a solid-state photodetector in which a photo-generated carrier can trigger an avalanche current due to the impact ionization mechanism. This device is able to detect low intensity signals (down to the single photon) and to discern the arrival times of the photons with a jitter of a few tens of picoseconds. SPADs, like avalanche photodiodes (APDs), exploit the photon-triggered avalanche current of a reverse biased p-n junction to detect an incident radiation. The fundamental difference between SPAD and APD is that SPADs are specifically designed to operate with a reverse-bias voltage well above the breakdown voltage (BV). This kind of operation is also called Geiger mode in literature, in analogy with the Geiger counter [6].

APDs and SPADs are purposely made to be operated at high electric fields in order to achieve an internal gain [3]. In reverse biased photodiodes, the electric field increases with the applied voltage, causing the increase of the drift velocity and of the kinetic energy of charge carriers injected in the depletion region. So, an electron (or a hole) can reach an energy high enough to break a bond when colliding with lattice atoms, thus generating a new electron-hole pair, and losing part of its energy in this process of impact ionization. Both the original carrier and the secondary electron and hole will be accelerated by the electric field and possibly contribute to the generation of more electron-hole pairs, resulting in a positive feedback loop (avalanche) which gradually increases the overall number of carriers. Note that this applies both to optically generated carriers and to carriers generated by any other mechanism (e.g., thermally generated carriers) [7]. The magnitude of the avalanche phenomenon is governed by two concurrent factors: the carrier ionization rates, which are defined as the number of pairs created by a carrier per unit distance travelled, and the rate at which electrons and holes leave the high-field

region and are collected at the device electrodes. Ionization rates strongly increase with the electric field [8].

Although silicon electrons have a higher ionization rate than holes, an electric field value of about $3 \times 10^5\ V/cm$ is required, on average, to create one electron-hole pair per 1 μm travelled. For bias voltages below the breakdown voltage, ionization rates are balanced by the extraction rate, therefore, carrier concentration and output current are increased by a finite multiplication factor, the gain, normally in the range between a few tens and a few hundreds. This is the case of APDs, which provide an output current proportional to the impinging light intensity. For bias voltages beyond the breakdown voltage, ionization rates are so high that the extraction rate does not keep pace with them, therefore, the carrier concentration and output current increase to very high values. This is the case of SPADs, whose gain reaches values $> 10^6$ [9, 10]. When a SPAD is biased beyond the breakdown voltage, it will stay in an OFF state for a short time, until a carrier (electron or hole) will trigger an avalanche event bringing the device into its ON state. The corresponding current pulse would be self-sustaining. Nevertheless, in order for the SPAD to be useful as a photodetector, the avalanche current must to be turned off by using proper quenching mechanisms, able to reduce the bias voltage below the breakdown value, and to finally restore it to its initial value, so that a new incoming photon can be detected [11]. In other words, the device operates in a binary mode and the need for quenching/recharging introduces a dead time between two consecutive events. The simplest way to quench the avalanche is by means of a high ohmic resistor in series with the SPAD, so that the voltage drop, caused by the avalanche current, lowers the SPAD bias down to the breakdown point.

1.3 The Silicon Photomultiplier

As previously reported in section 1.2, a single SPAD (operating in Geiger mode), functions as a photon-triggered switch, in either the ON or the OFF state, and therefore cannot provide proportional information regarding the magnitude of an instantaneous photon flux. Regardless of the number of photons interacting within a diode at the same time, it will ideally produce a signal of one impinging photon. In order to overcome this lack of proportionality, the Silicon Photomultiplier integrates an array of small, electrically and optically isolated Geiger mode photodiodes (Fig. 1.1) distributed with high density on a common substrate. Each photodiode element in the array is referred to a microcell. Typically numbering between 100 and 1000 per mm^2, each microcell has its own quenching resistor and is connected to a common analog output to produce a summation signal [7, 12] proportional to the number of detected photons [13–15]. It

detects photons identically and independently. The sum of the discharge currents from each of these individual binary detectors combines to form a quasi-analog output, and is thus capable of giving information on the magnitude of an incident photon flux.

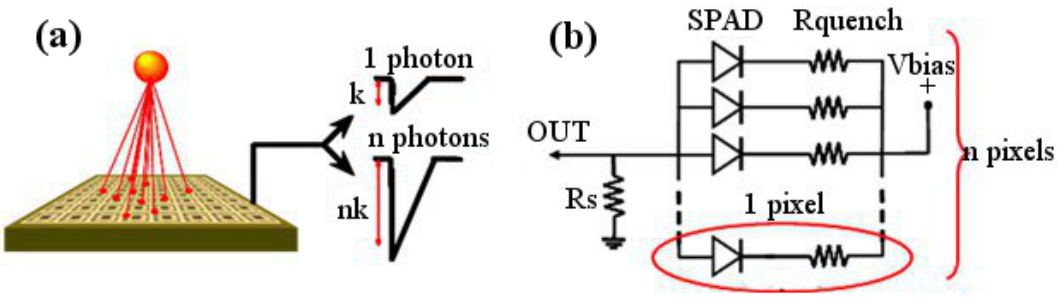

FIGURE 1.1: Operating principle (a) and equivalent electronic schematics (b) of silicon photomultiplier.

1.4 Main properties of the SiPM

- **Gain:** it is the number of electron-hole pairs created in the depletion layer of the device during an avalanche event. It is function of the overvoltage (OV) applied to the device and of the temperature. If compared to standard vacuum PMTs, SiPMs show a comparable gain ($> 10^6$) with a lower operating voltage (even <30 V for the SiPM versus several hundreds of Volts for the PMT) [2, 4].

- **Responsivity:** it measures the electrical output per optical input. It is expressed in units of amperes per watt of incident radiant power. Responsivity is a function of the wavelength of the incident radiation and of the sensor properties, mainly the bandgap of the material.

- **Photon Detection Efficiency (PDE):** it is given by the product of three parameters: the Quantum Efficiency (QE), the avalanche triggering probability, and the geometrical fill factor [13]. The QE is the ratio of the number of photogenerated carriers to incident photons. It depends on the wavelength. The triggering probability is the probability that an electron-hole pair in the depletion region triggers a self-sustaining avalanche. It depends on the position where the primary electron-hole pair is generated and on the overvoltage. The geometrical fill factor is the ratio of the active to the total area of the device. A dead area, around each microcell, is due to the presence of a virtual guard ring (made in order to reduce the electric field at the edge of the diode and ensure a uniform breakdown region in the central area of the microcell) and the structure preventing the optical cross-talk (described below) [13, 16]. The conversion between PDE and Responsivity of

a SiPM is achieved as follows (Eq. 1.1):

$$PDE_{\lambda} = \frac{Responsivity_{\lambda}}{G \times \lambda} \times \frac{hc}{e} \approx \frac{Responsivity_{\lambda}}{G \times \lambda} \times (1240\, W \times nm/A) \qquad (1.1)$$

where the Responsivity is in A/W, G is the gain, λ is in nm, h is the Planck constant, c is the speed of light in a vacuum, and e is the elementary charge.

- **Dynamic range:** it is the maximum number of photons that can be concurrently detected by the SiPM. The dynamic range is limited by the number of pixels. Indeed, regardless of the number of photons interacting within a diode at the same time, it will ideally produce a signal of one impinging photon (as previously observed in sections 1.2 and 1.3). Furthermore, during the recharging phase (time interval in which the OV on the pixels progressively increases from the value of breakdown to that of polarization) the SiPM detects photons with low efficiency, producing an output signal lower than the standard, and making the resolution of the charge spectrum worse. For this reason, the device works well only when the average number of impinging photons is low enough to permit every SiPM pixel to quench the avalanche pulse and recharge its diode capacitances before the same pixel is fired again (section 2.3.2).

- **Dark current:** it is the main source of noise limiting the SiPM performances. It mainly originates from carriers thermally generated in the depletion layer. Indeed, an avalanche can be triggered by an incoming photon or by any generation of free carriers. The latter produces dark counts with a rate of 100 kHz to several MHz per mm^2 at room temperature. Thermally generated free carriers can be reduced by cooling. Another possibility is to operate the SiPM at lower bias resulting in a smaller electric field and, thereby, lower gain. Furthermore, the dark counts can be reduced by minimizing the number of generation-recombination centers, impurities and crystal defects [3].

- **Optical crosstalk:** it is well-known that the avalanche process in silicon is accompanied by a photon emission process. Under the usual gain setting of a SiPM, the generated number of photons is large enough to parasitically trigger neighboring pixels. This effect degrades the amplitude resolution of a SiPM [3].

- **Electrical crosstalk:** some carriers, emitted from the junction of a pixel and diffusing to the epitaxial substrate, can reach the depletion region of the adjacent pixels. When it happens, they can trigger spurious avalanche events. Crosstalk can be reduced with a dedicated design of grooves between the cells which act as an electro-optical isolation. Operation at relatively low gain is advantageous.

- **Afterpulsing:** it is the last source of spurious counts and is due to charge carriers trapped within the semiconductor during the avalanche signal and later exponentially released [17]. Cooling the device results in an increase of the exponential decay constant, and therefore, the lowest operating temperature becomes a trade-off between the dark current and long-lasting afterpulse counts [18]. This could represent an intrinsic limitation to the implementation of large-area SiPM detectors, if one actually needs the single photon sensitivity. Nonetheless, the suitable use of SiPMs depends strongly on a particular application.

- **Recovery time:** the time needed to recharge a cell after a breakdown has been quenched. It depends mostly on the cell size (i.e., its capacity) and its quenching resistor. Afterpulses can prolong the recovery time because the recharging starts anew. This can be reduced operating at low gain. SiPMs need from one hundred of nanoseconds to hundreds of microseconds after a breakdown until the amplitude of a second signal reaches the same amplitude of the first signal. Mostly polysilicon resistors are used for the quenching of the avalanche event. They change their value with temperature, therefore, there is a strong dependence of the recovery time on the temperature [3].

1.5 SiPM, APD and PMT: a comparison

Current research in photodetectors is directed toward an increasing miniaturization of the pixel size, thus both improving the spatial resolution and reducing the device dimensions. On the other hand, measurements of low photon fluxes require high responsivity. In this scenario, SiPMs emerge as promising candidates and are considered an attractive possibility to replace both standard PMTs and conventional APDs. If compared to standard vacuum PMTs, SiPMs show higher QE, especially in the near infrared, low operating voltage (< 30 V) with a comparable gain ($> 10^6$), ruggedness, compact size and reduced sensitivity to temperature, voltage fluctuations and magnetic fields [2–4, 14, 15, 18, 19]. Furthermore, solid-state technology owns the typical advantages of the planar integration process: SiPMs can be manufactured at lower costs and with higher reproducibility with respect to PMTs [20, 21]. SiPMs show several advantages compared to APDs fabricated in conventional CMOS technology [22], such as: low bias voltage, higher responsivity and PDE in the visible and near infrared range, excellent single-photon response, fast rise time ($<<$ 1 ns) and low power consumption. Moreover, SiPMs have a much higher gain than APDs ($> 10^6$ versus $< 10^3$) [14]. Also, with reference to the integration process, they can be used in medical imaging systems

Design choice	**Consequence**
Semiconductor material	It has influence on the PDE and the range of wavelengths
P-on-N SiPM	Highest detection efficiency for blue light
N-on-P SiPM	Highest detection efficiency for red light
Thickness of the depleted layers	Range of wavelengths, optical crosstalk
Doping concentrations	Operating voltages
Impurities and crystal defects	Dark counts, afterpulses
Area of the cells	Gain, geometric factor, dynamic range, recovery time
Value of the quenching resistors	Recovery time, count rate/cell
Type of resistors	Temperature dependence
Optical cell isolation (trenches)	Crosstalk

TABLE 1.1: SiPM design choices and corresponding consequences on the operating parameters.

like Positron Emission Tomography (PET), Magnetic Resonance Imaging [23–27], Near-Infrared Spectroscopy (e.g., oximetry) [28, 29] and in immunoassay tests [30]. On the other hand, features like their high gain, fast timing response with low fluctuation and high responsivity to extremely low photon fluxes [21] could open up to new SiPMs applications in a variety of fields, such as very low power measurements (less than 1 pW) [31].

1.6 Choice of operating parameters

There are many different designs possible. In Tab. 1.1 a number of design choices are given together with the consequences on some operating parameters [32, 33].

In this work two types of SiPM technologies are presented: P-on-N and N-on-P [34]. Each one is characterized by its own typical spectral response: P-on-N structures exhibit a higher responsivity in the blue range, while N-on-P devices have a maximum in the red. For applications in positron emission tomography (PET), a higher sensitivity in the blue region is desirable, as the emission spectra of common PET scintillators peak in this part of the spectrum [15]. Therefore, P-on-N structures would be preferable. Otherwise, in applications like the near-infrared spectroscopy and calorimetry, the N-on-P silicon structure would be the best choice.

Many applications need the highest possible photon detection efficiency but they do not need high dynamic range (photon correlation studies, fluorescence spectroscopy, single electron LIDAR, neutrino detectors). Here, the best choice is a SiPM with P-on-N silicon structure, large cells, small value of the individual resistors and optical isolation between the cells. Other applications need large dynamic range (PET, scintillator readout, radiation monitors). The best is P-on-N silicon structure again, with small cells.

Chapter 2

The SiPM Responsivity in the Continuous Wave Regime

2.1 Introduction

SiPMs performances in photon counting mode have been investigated in several papers, using picosecond pulsed lasers [2–4, 12, 18–21, 35, 36]. Optical characterization performed via continuous wave (CW) sources has seldom been reported [31, 37, 38] even though this kind of excitation seems to be very useful in several applications. SiPMs could be employed as very sensitive optical power meters (down to hundreds of femtowatts), as very cheap sensors in the immunoassay tests and, above all, as sensors in the continuous wave near infrared spectroscopy systems for human brain monitoring [30, 31, 38–43].

Two types of technologies are used in SiPMs: P-on-N or N-on-P [34, 44]. Each one is characterized by its own typical spectral response: P-on-N structures exhibit a higher responsivity in the blue range, while N-on-P devices have a maximum in the red.

In this chapter is reported the electrical and optical comparison, in CW regime, of two novel classes of SiPMs fabricated in planar technology on silicon P-type and N-type substrates, respectively. In particular, I will describe their characterization in terms of I-V curves, responsivity and range of linearity. Responsivity measurements have been performed with an incident optical power from tenths of picowatts to hundreds of nanowatts and on a broad spectrum, ranging from ultraviolet to near infrared (340-820 nm).

2.2 Description of the devices

SiPM fabrication technology is based on a single-photon avalanche diode (SPAD) cell. The N-on-P (P-on-N) SiPM structures investigated in this work are fabricated on P-type (N-type) silicon epitaxial wafers and formed from planar $N^+ - P$ ($P^+ - N$) microcells. A polysilicon quenching resistor is integrated inside each cell. Thin optical trenches, filled with oxide and metal, surround the microcell active area to reduce cross-talk effects between adjacent pixels. Hereinafter, I will describe the physical structure of a typical N-on-P SiPM, since, to a large extent, the process flow of P-on-N SiPMs is obtained by inverting the doping of the layers of standard N-on-P technology.

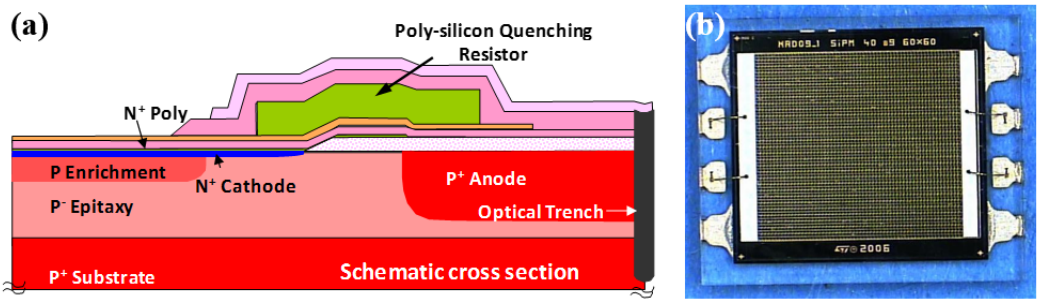

FIGURE 2.1: (a) Schematic cross section of the N-on-P SiPM cell; P-on-N SiPM is obtained by inverting the doping of the layers. (b) Optical microscopy picture of the large area SiPM in SMD package.

The N-on-P device features a 3.5 mm x 3.5 mm active area (3600 microcells, 45 % fill factor and 58 μm cell pitch) enclosed in a 5 mm x 5.5 mm package. Fig. 2.1(a) shows a sketch of the device cross section, while in Fig. 2.1(b) an optical microscopy image of a large area SiPM investigated is reported. A N-P junction is fabricated on silicon epitaxial P-type wafers through a planar process and it operates with a reverse biased voltage, well above the breakdown value (Geiger mode). The anode is defined through a boron implanted P-layer that forms an enrichment region in each microcell, thus fixing the junction breakdown voltage. The anode is surrounded by an implanted P+ sinker, that is connected to a bonding pad; hence it can be biased either from the back or from the front side. The cathode is a 0.2 μm thin N+ polysilicon layer, doped with an arsenic diffusion, deposited on the top of the structure [45].

The passive quenching circuit is a low doped polysilicon resistor. The latter is present in every single cell around the cathode [45] and has a typical value of 256 $k\Omega$ (273 $k\Omega$) for the N-on-P (P-on-N) SiPM. Other features of the fabricated devices are: a thin junction depletion layer (about 1 μm thick); a reduced thickness (about 0.15 μm) of the quasi-neutral region above the space charge region, in order to increase the absorption

efficiency in the blue wavelength range; a suitable structure for optical isolation consisting of thin trenches (1 μm wide) filled with tungsten and oxide and surrounding the active area of each microcell [45]. Moreover, dedicated gettering techniques have been integrated into the manufacturing process to reduce the defectivity in the active area [21]. Emission microscope pictures with different magnification, reported in Fig. 2.2, show the avalanche turn-on phase in a typical N-on-P SiPM kept in dark condition and reverse biased at 3 V above the breakdown voltage.

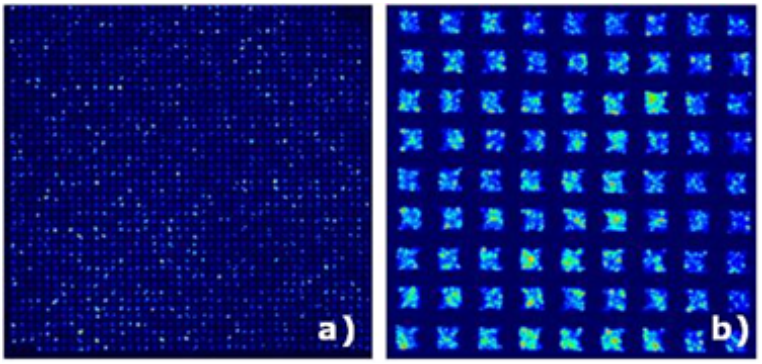

FIGURE 2.2: Emission microscope pictures with low (a) and high (b) magnification factor obtained on a 3.5 mm x 3.5 mm SiPM reverse biased at 3 V above the breakdown voltage.

Such images were acquired by means of a Hamamatsu PHEMOS-1000 photon emission microscope and applying a positive voltage to the SiPM common cathode metallization, while the anode metallization was set at ground. It is worth noting the absence of hot-spots in the microcells when the avalanche multiplication occurs with a bias just a few volts above the breakdown value.

2.3 Experimental results and data analysis

2.3.1 Electrical characterization

Measurements of SiPM forward and reverse current, breakdown voltage and leakage current were performed using a semiconductor parameter analyzer (Keithley 2440) at controlled room temperature and in dark conditions. Fig. 2.3 shows the reverse I-V characteristics for both the types of investigated structures. Breakdown voltage was measured to be 28.0 V and 27.3 V for N-on-P and P-on-N SiPMs, respectively. The slope of the linear region in the forward I-V characteristic (shown only for the N-on-P SiPM in Fig. 2.4) allowed us to extrapolate the value of 256 $k\Omega$ (273 $k\Omega$) for the quenching resistor of each single N-on-P (P-on-N) microcell [46].

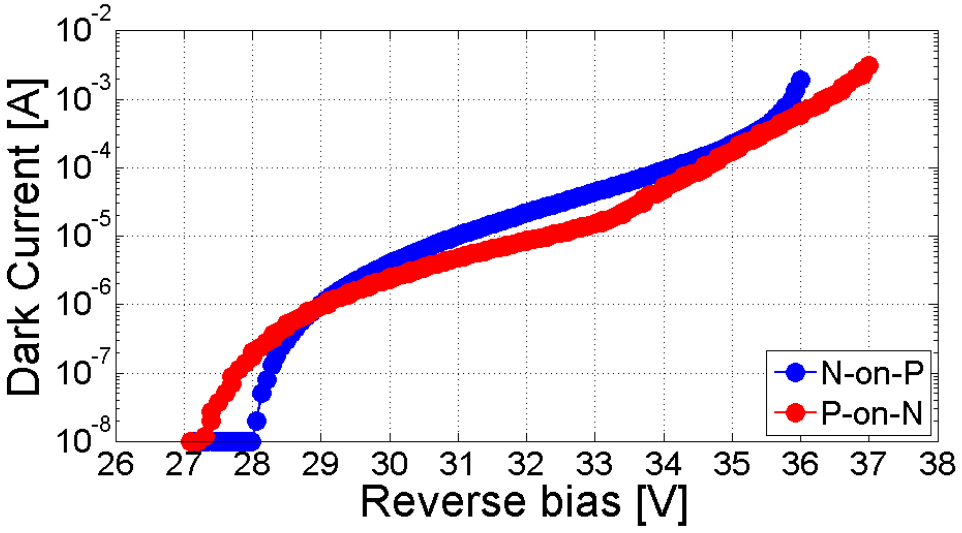

FIGURE 2.3: Reverse I-V characteristics for N-on-P and P-on-N SiPMs, measured at room temperature and in dark conditions.

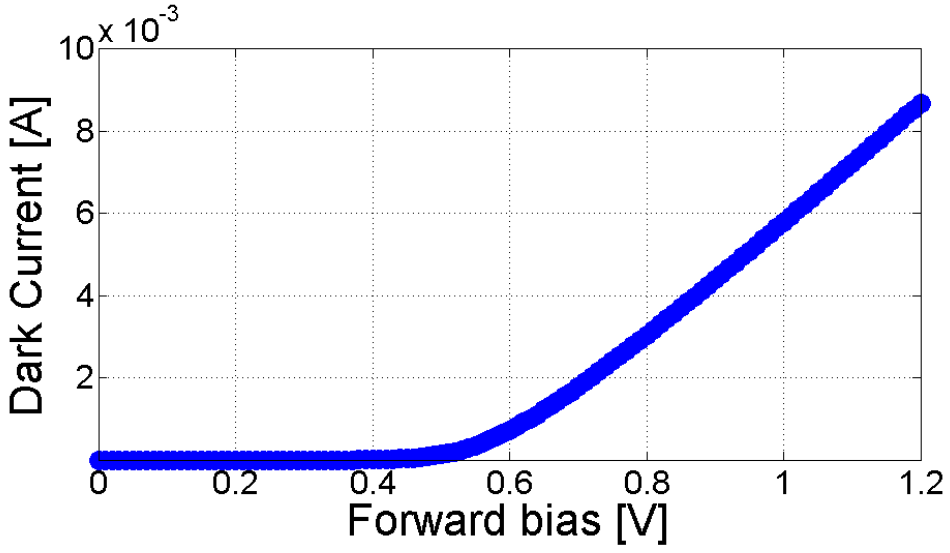

FIGURE 2.4: Forward I-V characteristic for the N-on-P SiPM, measured at room temperature and in dark conditions.

2.3.2 Responsivity measurements as a function of the incident optical power

Herein, I refer to the responsivity as the ratio of the SiPM output current (net of the dark current) and the incident optical power without any normalization on the SiPM gain. In order to explore the linear behavior of the devices, I first performed SiPM responsivity measurements as a function of the incident optical power. Experimental setup is shown in Fig. 2.5.

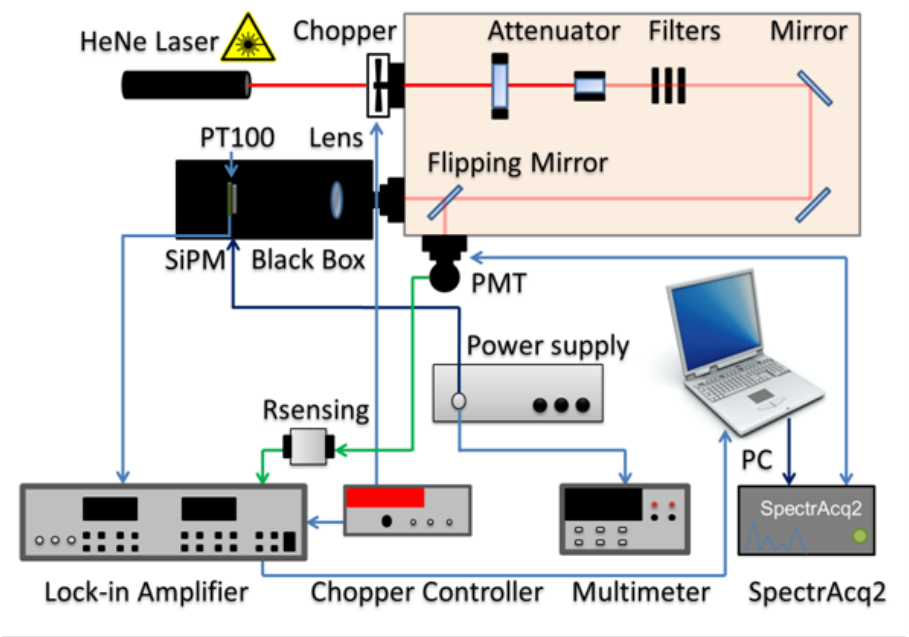

FIGURE 2.5: Sketch of the experimental setup for measurements of SiPM responsivity versus incident optical power.

The optical power provided by a HeNe laser ($\lambda = 632.8$ nm) was attenuated by means of some neutral density filters and controlled through a half-wave plate and a Glan-Thompson cube polarizer. This system allowed us to fine tune the optical power down to sub picowatts. The laser beam was chopped at 183 Hz and was sent -depending on the position of a flipping mirror- either on the active area of the SiPM under test or on a reference PMT (Hamamatsu R928), previously calibrated and used to estimate the optical power incident on the SiPM. The latter was biased using a stabilized power supply and a SMD resistor (100 Ω, sensing resistor), connected between the cathode and the ground. Unlike what several papers report for pulsed measurements [18, 21], I did not include any other resistor in the bias line. In fact, this resistor, together with the capacitors of the SiPM itself (or capacitors eventually present in the biasing circuit), could behave as a low-pass filter for the SiPM response. This would limit the linear response of the device, when working in the continuous wave regime and on a wide

range of incident optical powers. The SiPM and the biasing circuit were located in a metal black box, being thus shielded by ambient light and electromagnetic noise. A 25 mm focal length lens was placed between the flipping mirror and the SiPM, making sure that the light spot covered the whole active area of the device. During measurements, the temperature of the SiPM package was monitored with a PT100 thermistor placed in the back side of the device. In order to perform low optical power measurements, a lock-in amplifier was connected to both the SiPM and the PMT outputs, while a readout system (SpectrAcq2) digitalized the signal and allowed data acquisition.

The setup described above was the same for the whole duration of the tests, ensuring that all experiments were reproducible and all data consistent to each other. The SiPM was biased at increasing external bias and the responsivity peak (i.e., maximum output current, net of the dark current) was found applying a reverse bias of 35.3 V between cathode and anode. Responsivity measurements were performed at controlled room temperature and are plotted in Fig. 2.6 for the N-on-P SiPM and in Fig. 2.7 for the P-on-N, while the trend of the temperature of the SiPM package as a function of the incident optical power is shown, respectively, in Figs. 2.8 and 2.9.

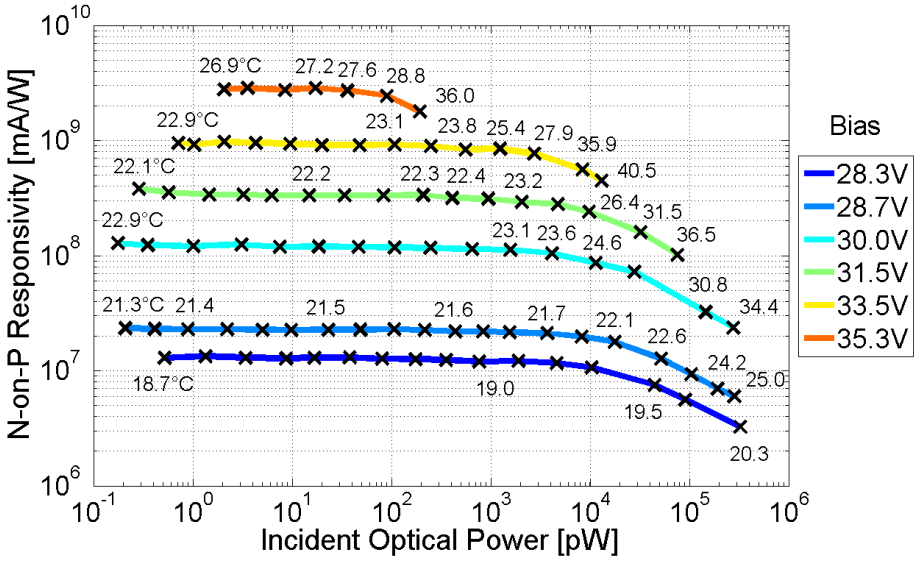

FIGURE 2.6: N-on-P SiPM responsivity vs incident optical power at $\lambda = 632.8$ nm obtained at different supply voltages and monitoring the temperature of the SiPM package.

I will refer only to the N-on-P technology below in this section, given that similar considerations apply to the P-on-N. It is worth noting that responsivity shows a flat response up to a power level which depends on the applied bias. In more detail, the linear behavior of the device extends up to about 10 nW for a bias of 28.3 V, while it is reduced when the reverse bias voltage increases. In the flat region of each curve the

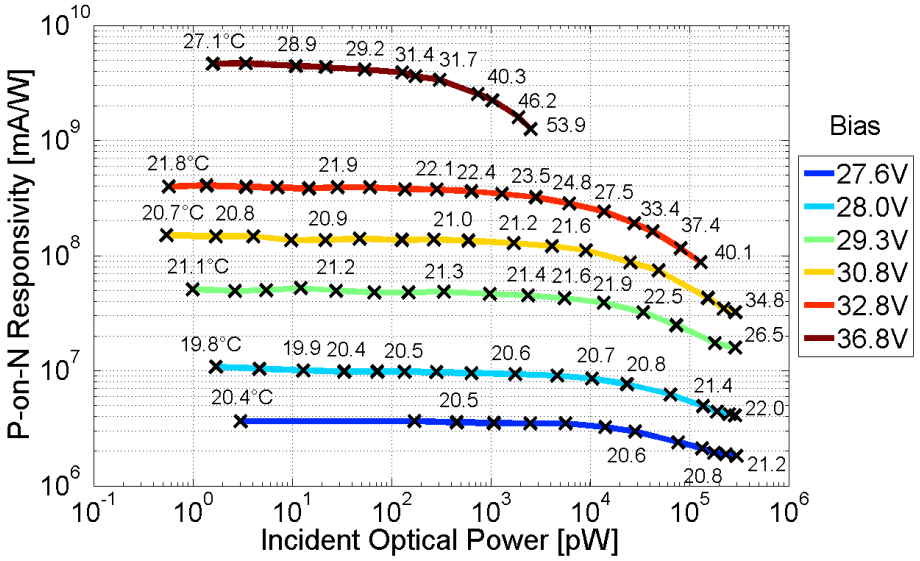

FIGURE 2.7: P-on-N SiPM responsivity vs incident optical power at λ = 632.8 nm obtained at different supply voltages and monitoring the temperature of the SiPM package.

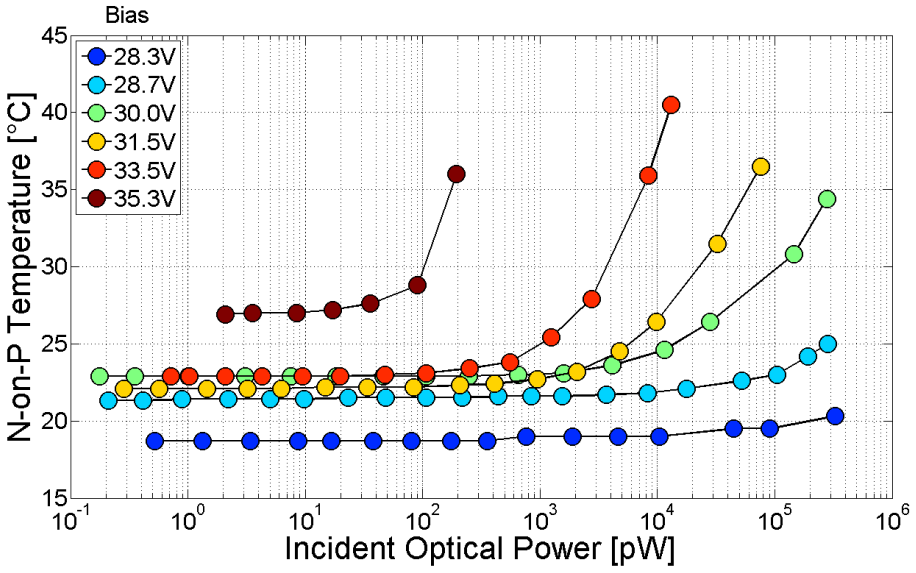

FIGURE 2.8: Temperature of the N-on-P SiPM package vs incident optical power at λ = 632.8 nm and at different reverse bias voltages.

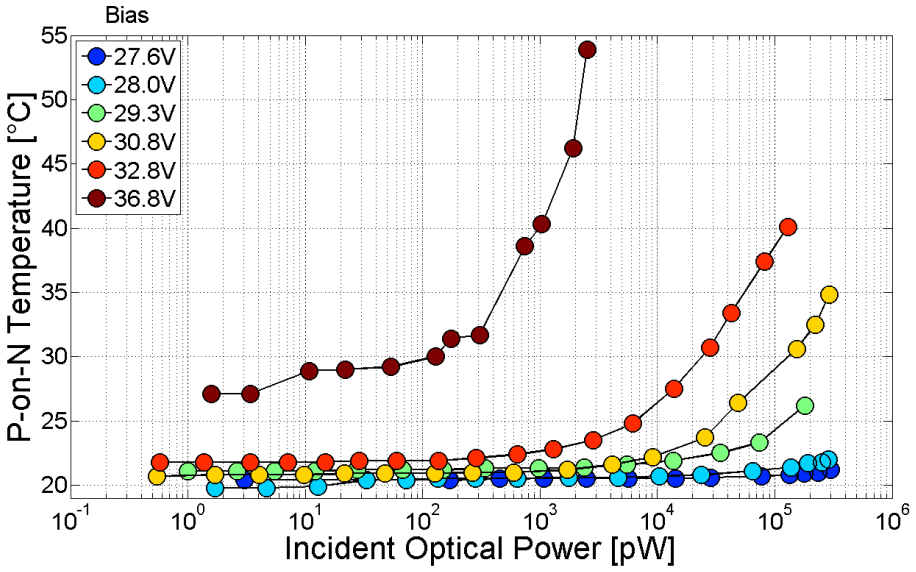

FIGURE 2.9: Temperature of the P-on-N SiPM package vs incident optical power at λ = 632.8 nm and at different reverse bias voltages.

measured temperature of the SiPM package was approximately constant (around room temperature), while it increases in the region corresponding to the slope of the curves (Fig. 2.8). This temperature difference is quite small for lower biases ($\Delta T < 2$ °C for a bias of 28.3 V and $\Delta T < 4$ °C for a bias of 28.7 V) while it strongly increases for higher bias voltages ($\Delta T \approx 18$ °C for a bias of 33.5 V). The measurement was also repeated at 28.3 V (corresponding to the maximum flat response) reducing the value of the sensing resistor to 50 Ω, in order to ensure that the SiPM linear response is not influenced by its value. I confirmed that the responsivity turnover occurs at the same optical power (Fig. 2.10).

All the errors were taken into account and propagated, although the dominant contribution came from the indetermination of the PMT calibration curve (calibration uncertainty = 5 %). Measurements were carried out using a battery power supply, in order to remove possible power line interferences. As written above, SiPM output currents, used to evaluate the responsivity, are net of the dark current. In particular, the PMT dark current was negligible in all performed measurements, while the SiPM dark current was automatically discarded by the lock-in amplifier since it is not chopped. As previously observed, the linear range extends up to about 10 nW for a bias of 28.3 V. This result takes into account a maximum deviation of 15% from the linear trend, detected at low incident powers (< 10 pW). This is shown in Fig. 2.11 where I plotted the relative residuals ((measured responsivity *minus* responsivity mean value in the flat region) *divided by* responsivity mean value in the flat region) of the N-on-P SiPM responsivity vs

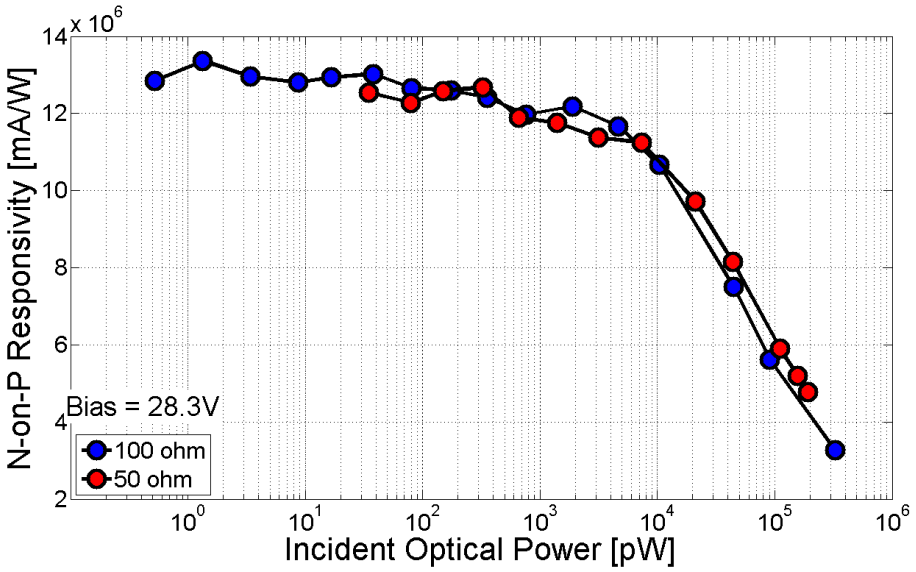

FIGURE 2.10: N-on-P SiPM responsivity versus incident optical power, biasing with two different values of the sensing resistor (50 and 100 Ω), at $\lambda = 632.8$ nm and at 28.3 V.

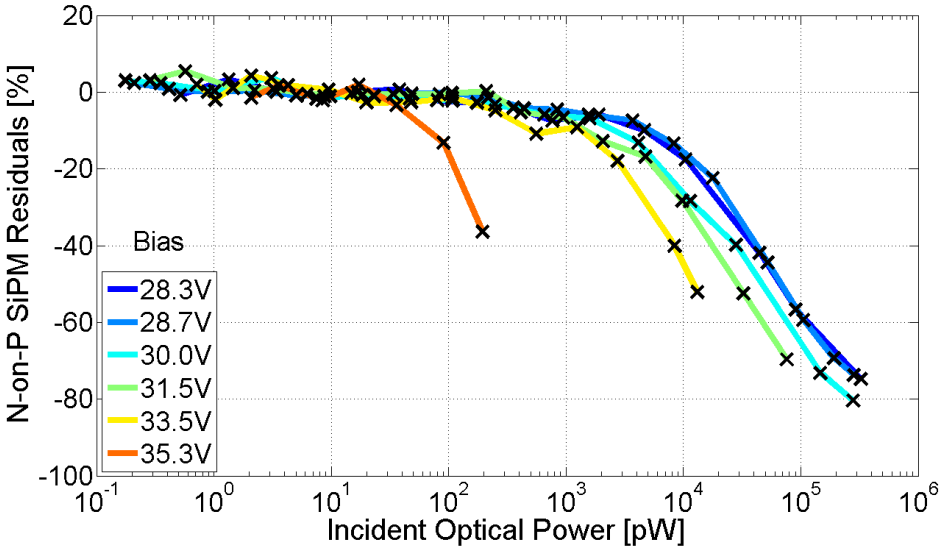

FIGURE 2.11: Relative residuals of the N-on-P SiPM responsivity as a function of the incident optical power.

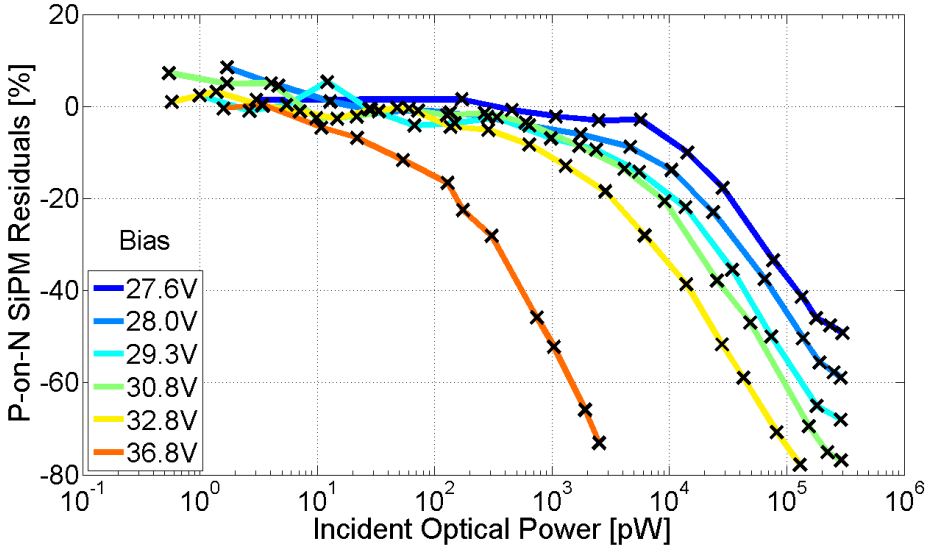

FIGURE 2.12: Relative residuals of the P-on-N SiPM responsivity as a function of the incident optical power.

incident optical power. The linear range is strongly reduced at increasing biases (up to 100 pW at 35.3 V). Fig. 2.12 depicts similar results for the P-on-N technology.

Measurements of responsivity as a function of the incident optical power can be explained as follows. The sum of the photon rate and the dark rate in the flat regions are low enough to permit every SiPM cell to quench the avalanche pulse and recharge its diode capacitances (through its quenching resistor) before the same cell is fired again (because another photon hits it again or because a dark event occurs; details about the SiPM electrical model can be found in [45]).

Fig. 2.13 depicts SiPM responsivity versus the rate of firing cells (obtained dividing the SiPM overall current, sum of the dark current and the photocurrent, by the product of the SiPM gain and the elementary charge) for this class of SiPMs, at $\lambda = 632.8$ nm and at different reverse bias voltages. I observe the responsivity turnover occurs at the same value except for the 35.3 V bias. This indicates that the responsivity is mainly limited by the finite number of cells that are fired by both photon rate and dark rate, up to the bias of 33.5 V.

At the lowest biases (i.e., 28.3 V and 28.7 V), in correspondence to 10 nW, the dark current is very low (the photon current is about 100 % of the overall current) and the responsivity begins to decrease mainly because of a pile up effect of the incoming photons during the recharging phase of the SiPM microcells. In fact, during this time, the device is not completely blind to the absorption of photons, but it is able to detect incident light -after the quenching of each avalanche event- showing a triggering efficiency and a gain

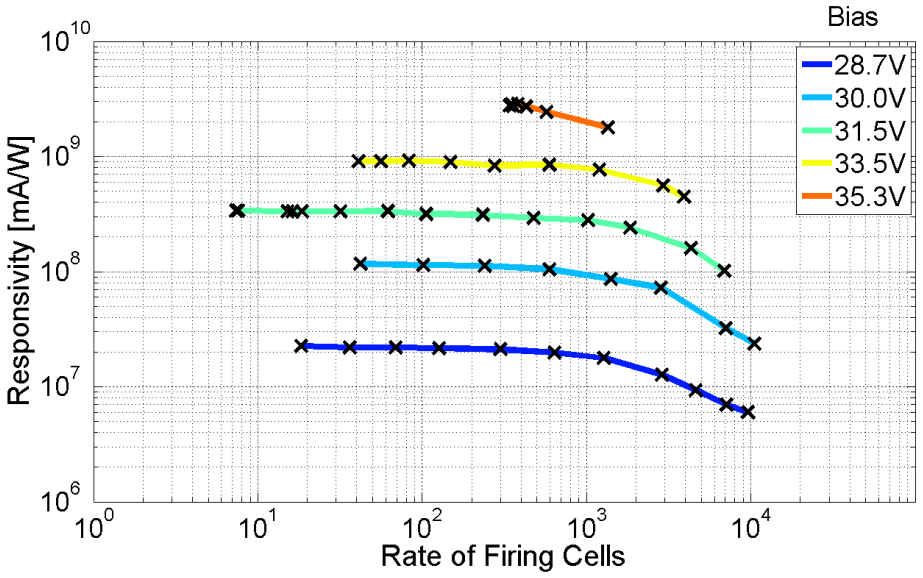

FIGURE 2.13: N-on-P SiPM responsivity versus rate of firing cells, at $\lambda = 632.8$ nm and at different reverse bias voltages.

directly proportional to the overvoltage (OV) at the junction. The amount of charge produced by the microcells, when fired by photons absorbed during the recharging time, is lower than that delivered when the recharging at the depletion layer is complete. Furthermore, for high impinging photon fluxes, the probability that photons can be absorbed by microcells in the recharging phase is higher, due to the limited number of cells in the array. The combination of these effects gives rise to the saturation of the output current, that leads to the responsivity decrease, as shown in the curves at 28.3 V and 28.7 V (Fig. 2.6).

Increasing the bias (from 30.0 V to 33.5 V), I observed the rise of the dark current due to the rise of the temperature of the SiPM package. The latter is caused by the increase of the waste power, that is particularly evident at the highest incident optical powers (in correspondence to the responsivity slopes), as shown in Fig. 2.8. The photon current decreases down to 82.6 % of the overall current, in correspondence to the turnover at 33.5 V. The rise of the dark current, mainly caused by thermal noise, busies the limited number of the SiPM cells and represents the main cause of the early responsivity decrease at the highest biases up to 33.5 V. Furthermore, as the optical power increases, the photocurrent linearly grows because of the SiPM high gain. As a consequence, the device temperature increases (Fig. 2.6), thus raising the breakdown voltage with a measured rate of about 30 mV/°C. This measurement was performed locating the SiPM in a black box (dark conditions) and employing a semiconductor parameter analyzer (Keithley 2440). The atmosphere inside the black box was dried using silica gel. The

temperature of the SiPM package was controlled through a Peltier cell, placed in the back side of the device, and monitored through a PT100 thermistor.

The growth of the breakdown voltage corresponds to a lower overvoltage on the junction that leads to a gain (and hence responsivity) reduction. The measured shift of the breakdown voltage, in correspondence of the responsivity turnover and considering the lowest measured temperature (19 °C) as the reference temperature, is only about 300 mV at 35.3 V (worst case) and absolutely negligible (less than 1 mV) at 28.3 V (best case). Anyway, this is a secondary effect that could not explain alone the responsivity turnover. In fact, as shown in Fig. 2.14, if the responsivity always turns over at the same waste power, it would support the idea of a temperature dominated turnover (assuming the waste power proportional to the temperature), but it does not.

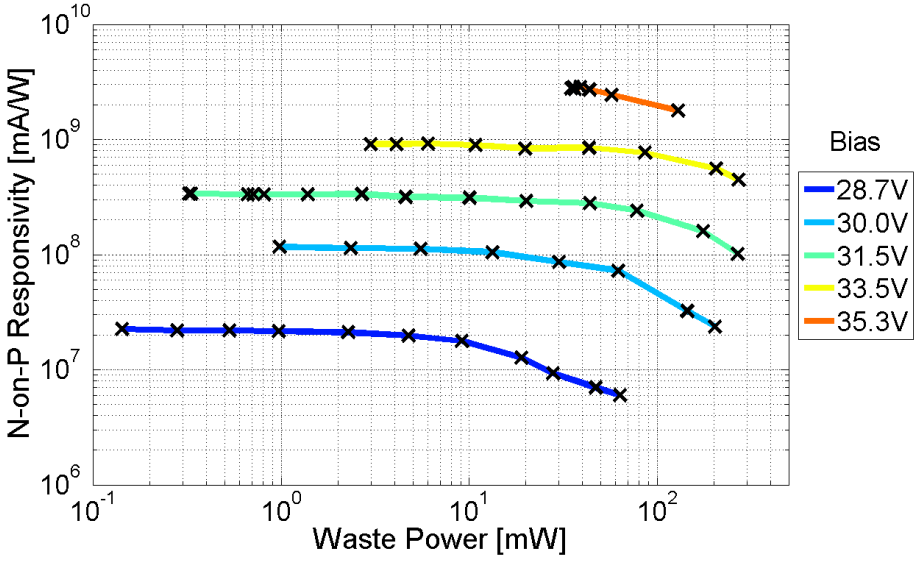

FIGURE 2.14: N-on-P SiPM responsivity versus waste power, at $\lambda = 632.8$ nm and at different reverse bias voltages.

Responsivity at 35.3 V was measured up to 200 pW. This curve represents a critical condition for the device in terms of dark current (Fig. 2.3) and temperature (Fig. 2.8). The percentage of the overall current due to the photon rate, in correspondence to the responsivity turnover at 35.3 V, is only 13.6 %, very low if compared to the one measured at lower biases. The responsivity turnover at 35.3 V is not aligned to those at the other biases (Fig. 2.13) because of the strong increase of the current flowing through the junction: indeed, this current is too high to ensure quenching. For this reason, the device is working outside of the usual operation range, i.e. when the quenching resistors sufficiently limit the current during breakdown.

I also estimated the average number of fired cells N_t corresponding to a responsivity deviation of 20 % from the linear trend (unlike the previous definition of linear range, up to 15 %), in order to make a comparison with the pulsed mode, as reported in literature [46]. I considered a temporal window (Δt) equal to the recovery time of each SPAD. I indicate with N the number of cells that contribute (even partially), within this time interval, to the overall charge (Q) and with q the maximum charge stored by each SPAD at a given bias, obtained multiplying the equivalent SPAD capacity ($\approx$ 175 fF, typical value for this SiPM class) and the applied overvoltage. Q can be evaluated by multiplying the measured overall current I (that is an average current) and the recovery time (Eq. 2.1):

$$Q = I \times \Delta t \tag{2.1}$$

Unlike the pulsed mode, in which all the cells are triggered by the laser pulse at the same time, in my CW case, the cells are randomly fired, so their charge pulses are uniformly distributed in time. Hence, within Δt, each fired cell contributes, on average, with $q/2$ to Q. Therefore the number of fired cells is given by Eq. 2.2:

$$N = \frac{Q}{\frac{q}{2}} = \frac{2 \times I \times \Delta t}{q} \tag{2.2}$$

The previous expression was calculated in correspondence of each turnover condition, for all the biases employed in my measurements and assuming Δt = 220 ns. So N_t was obtained as the ratio of the overall average current supplied by the SiPM and the current corresponding to the single SPAD pulse. I found the same value ($N_t \approx 1500$) for all the biases, with the only exception of the 35.3 V bias, in which $N_t \approx 700$. This further supports the hypothesis that the responsivity is limited by the dynamic range (number of cells) of the SiPM up to 33.5 V and that the turnover condition occurs when about 42 % of cells are fired. This condition is quite close to the common definition of the maximum usable range of SiPM in pulsed mode, i.e., when 50 % of cells are fired [46]. A more practical parameter to define this usable range in the CW regime is the maximum ratio of the overall current and the applied overvoltage. For the N-on-P device this parameter resulted around 0.6 mA/V (Fig. 2.15).

The measured dependence of the responsivity with respect to the incident optical power permits to use the SiPM as a very sensitive power meter with a dynamic range from sub picowatts to several nanowatts, for lower reverse biases [31]. This is an outstanding feature that can be exploited, for example, in those medical imaging systems where such a huge dynamic range is mandatory, being the detected optical power significantly variable with the distance between the detector and the source [42].

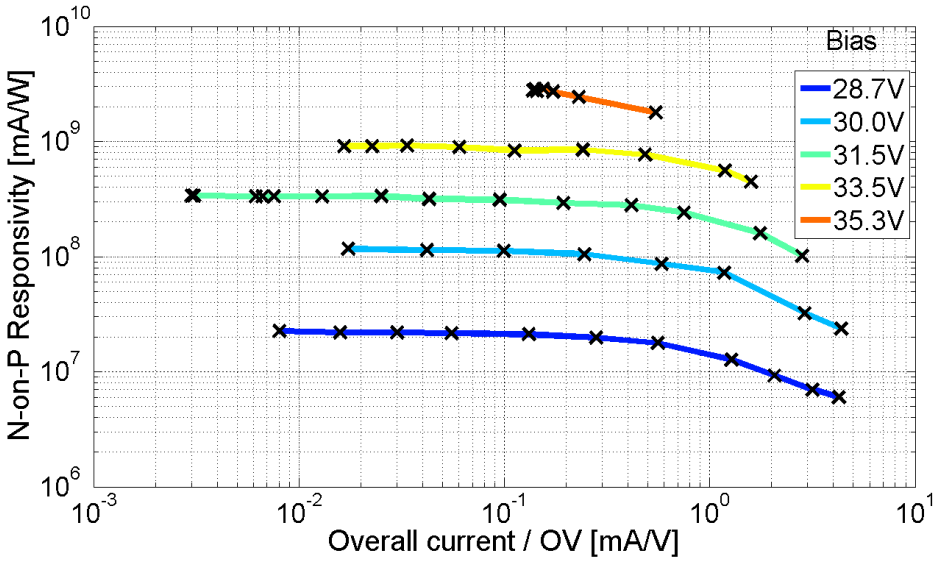

FIGURE 2.15: N-on-P SiPM responsivity versus the ratio of the overall current and the applied overvoltage, at $\lambda = 632.8$ nm and at different reverse bias voltages.

2.3.3 Spectral characterization

In order to evaluate the SiPM responsivity on a broad spectrum and at different bias voltages, I used the setup in Fig. 2.16. The white light coming out from a xenon lamp

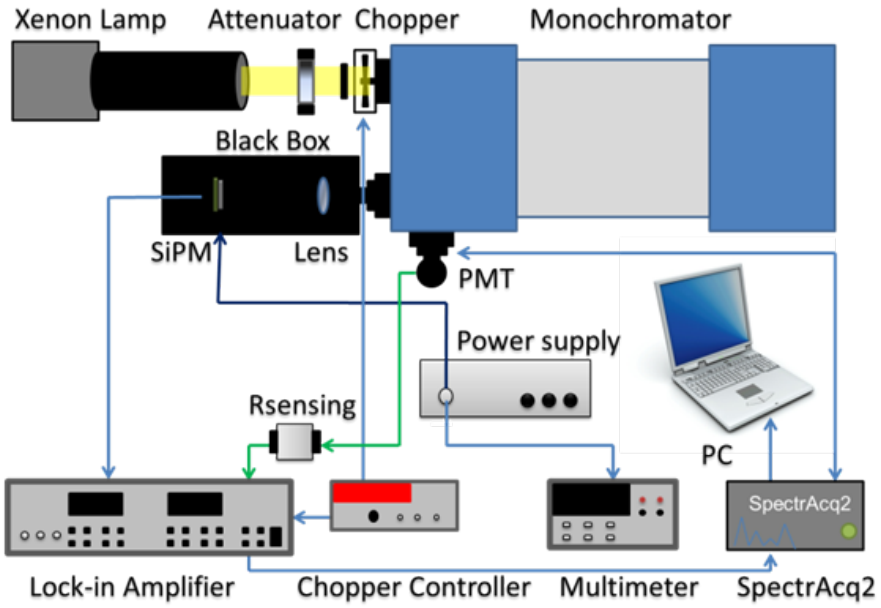

FIGURE 2.16: Sketch of the experimental setup for measurements of SiPM responsivity vs wavelength.

was attenuated via a circular variable neutral density filter and spectrally filtered by a

monochromator. The output monochromatic light was sent to the SiPM under test or to the reference PMT, according to the position of a flipping mirror placed inside the monochromator and controlled via software. As in the case of measurements reported in the previous section, the SiPM and its biasing circuit were located in a metal black box and a lock-in amplifier was used to reduce noise. In order to obtain a uniform illumination of the SiPM active area, I set the slit widths of the monochromator at 1 mm (corresponding to a spectral resolution of about 2 nm) and used a 25 mm focal length lens. Spectral measurements were performed from 340 to 820 nm, with a wavelength step of 2 nm.

The attenuated optical power of the xenon lamp, incident on both the PMT and the SiPM, spanned over the 60 - 100 pW range, in order to let the SiPM work in the linear region (see Figs. 2.6 and 2.7). I employed some narrowband filters (FWHM = 10 nm) placed in front of the exit slits, to verify that second orders of unwanted light (diffracted by the grating in the same position) were negligible and did not invalidate my measurements.

Responsivity was calculated dividing the SiPM photogenerated current by the incident optical power, the latter being estimated from the calibrated PMT photogenerated current. The same considerations concerning the dark current, reported in section 2.3.2, apply: it was negligible for the PMT, while it was automatically discarded by the lock-in amplifier for the SiPM. In Fig. 2.17 I report my responsivity measurements for the

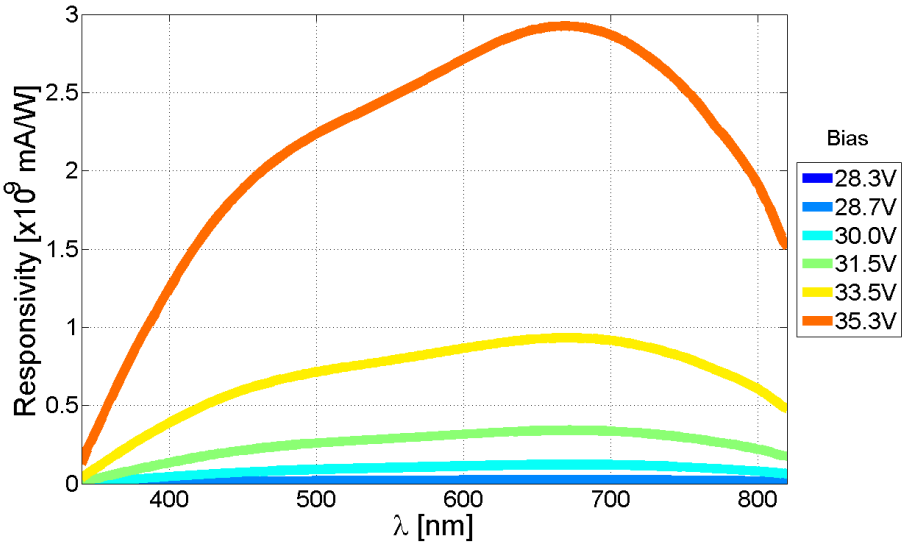

FIGURE 2.17: N-on-P SiPM responsivity vs wavelength at different reverse bias voltages.

N-on-P device, carried out in the abovementioned spectral range and at different reverse bias voltages, showing a peak around 669 nm. As expected, I found the highest values

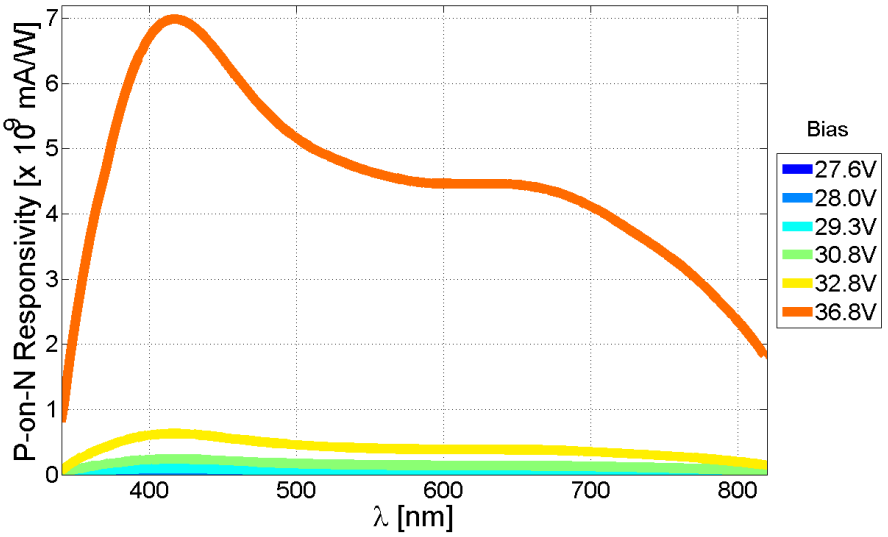

FIGURE 2.18: P-on-N SiPM responsivity vs wavelength at different reverse bias voltages.

of responsivity for the same bias reported in section 2.3.2 (35.3 V) with a maximum value of about 2.9 $\times$ 10^9 mA/W. Fig. 2.18 reports the responsivity measurements for the P-on-N device, showing a peak at 416 nm corresponding at a value of about 7.0 $\times$ 10^9 mA/W. In Figs. 2.19 and 2.20 I also show the same responsivity measurements,

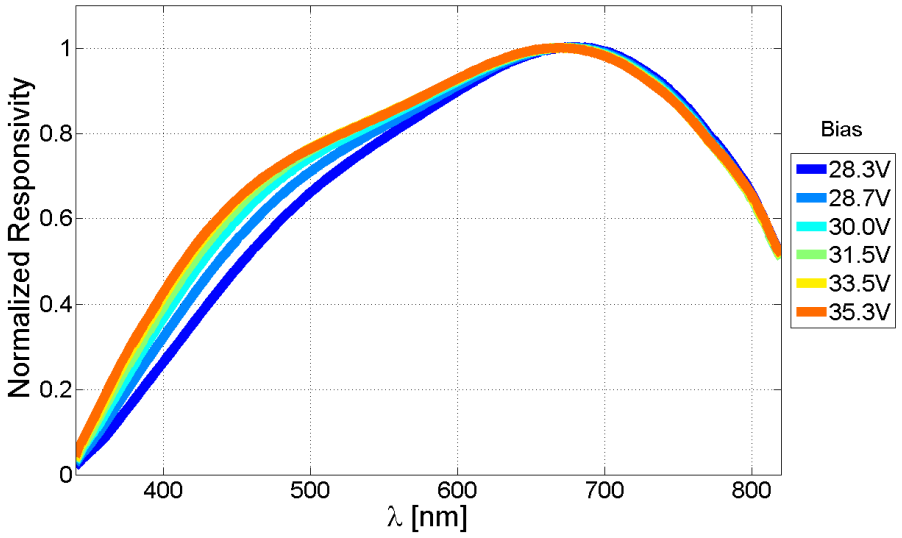

FIGURE 2.19: N-on-P SiPM responsivity vs wavelength at different reverse bias voltages, each one normalized at its value at 669 nm.

normalized at their values at, respectively, 669 nm and 416 nm, to better highlight how the spectral shape changes at different biases.

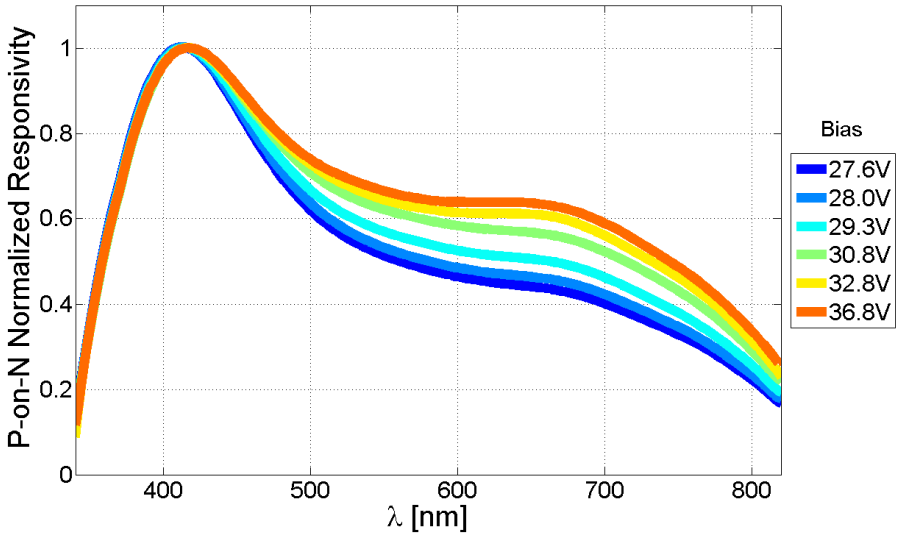

FIGURE 2.20: P-on-N SiPM responsivity vs wavelength at different reverse bias voltages, each one normalized at its value at 416 nm.

The measured wavelength dependence of the N-on-P SiPM responsivity can be explained as follows. Most of the power in the blue light range is absorbed within the first 200 nm of silicon, i.e. most photons in this range are absorbed in the quasi neutral region (about 150 nm thick) above the depletion region of the device. Only some of the holes produced by the blue photons diffuse into the high field region and trigger the avalanche with a considerably lower probability than for an electron. The responsivity peak is in the red light range, thanks to the contribution -to the total measured signal- of the minority carriers (i.e., the electrons) photogenerated in the p-doped epitaxial layers below the junction depletion layer (down to about 3 μm). These carriers can in fact drift towards the lower edge of the depletion layer before being accelerated by the electrical field and, in case, trigger the avalanche pulse. It is well known that the electrons in silicon have a higher diffusivity and impact ionization rates than holes and this makes noteworthy their contribution to the measured signal. In Fig. 2.19, I observe that the responsivity remains substantially unchanged at increasing bias voltages, with a slight increase in the blue range. At increasing biases the depletion region of each SPAD widens in the n-doped layer, being the p-doped layer fully depleted once the cell is biased above the breakdown. The spectral changes in the blue are due to a decreasing thickness of the N+ Poly layer. Thus, more holes have a chance to get into the avalanche region and, above all, the probability that these holes produce a breakdown increases.

Light in the near infrared range penetrates deeper into the non-depleted bulk, reducing the probability of reaching the depletion region due to the higher recombination (typical diffusion lengths are $\approx$ 10 μm) [32, 47–49]. The responsivity increases with the bias

voltage in the linear region of the reverse I-V characteristic (Fig. 2.3), while it decreases in the saturation region (i.e., reverse bias above 35.3 V) because of the strong rise of the dark current (curves are not shown). In the P-on-N device (Figs. 2.18 and 2.20), shorter wavelength (blue) photons, due to their higher absorption in silicon, will tend to interact in the first p-type layer, producing electrons (i. e. minority carriers) that move toward the junction under the influence of the electric field. Conversely, longer wavelength (red) photons travel deeper into the material and will tend to be absorbed by the N layers, and the generated holes will drift toward the junction. The trigger efficiency is then reduced [44]. P-on-N structures thus exhibit a higher responsivity at shorter wavelengths.

Such a responsivity response, together with low cost, low supply voltage, high gain and low noise of the SiPMs, makes them good candidates for a variety of applications (e.g. oximetry, immunoassay and PET).

2.4 Conclusions

In this chapter I reported the electrical and optical characterization, in CW regime, of two novel (3600 channels) P-on-N and N-on-P SiPM classes. In particular, I have reported SiPM responsivity measurements as a function of the incident optical power from hundreds of nanowatts down to sub picowatts, at $\lambda = 632.8$ nm, monitoring the device package temperature. I found that responsivity exhibits a flat region whose extension depends on the applied reverse bias voltage. The linear behavior of both classes of devices extend up to about 10 nW for the lowest applied biases, while it is reduced when the reverse bias voltage increases.

As regards the N-on-P class, I demonstrated that, up to a bias of 33.5 V, the responsivity decreases because of the limited number of cells that are fired by the photon rate and the dark rate. At higher biases other phenomena occur, thus further reducing the linear range. Similar results apply to the P-on-N class. These measurements allowed to define an innovative criterion to estimate the average number of fired cells in CW regime and to establish the conditions necessary for the device to be usable in that regime. Results show the outstanding performances of the fabricated SiPMs even at very low photon fluxes and low bias voltages.

Moreover, responsivity measurements on a broad spectrum and at different reverse bias voltages were shown: I found the responsivity peaks in the red and in the blue ranges for the N-on-P and the P-on-N classes, respectively. A physical interpretation of all the responsivity results was also provided.

Chapter 3

SNR Measurements of SiPMs in the Continuous Wave Regime

3.1 Introduction

Most of the current literature covers the usage of SiPMs for single photon counting, using picosecond pulsed lasers [2–4, 12, 18–21, 35, 36] and, therefore, the dark noise is the main noise source. However, applications like NIRS [30, 31, 38–43] require the usage of SiPMs in the CW regime and for analog mode measurements. Measurements of low photon fluxes require high responsivity and a remarkable Signal-to-Noise Ratio (SNR). Therefore, even if it has been scarcely discussed, it is crucial to analyze the SNR also in CW conditions, putting in evidence the main differences with the pulsed regime. Indeed, when operating with CW light with very low intensities, the shot noise resulting from statistical fluctuations of the photons has to be considered [50–52].

In this Chapter, the SNR performances have been studied in the CW regime of the N-on-P SiPM presented in chapter 2. In particular, SNR measurements were performed as a function of the applied bias, of the reference frequency and of the temperature of the SiPM package. Also, similar measurements were performed on a PMT, in order to make a comparison.

3.2 Experimental results and data analysis

In the following measurements, SNR of SiPMs is given by the ratio of the photogenerated current, filtered and averaged by a lock-in amplifier, and the rms deviation of the same current. I employed a 10 Hz equivalent noise bandwidth, around the lock-in amplifier

reference frequency. The measured noise takes into account the shot noise, resulting from the photocurrent and the dark current, while background light is not present in my setup.

The experimental setup is shown in Fig. 3.1. The optical power provided by a HeNe laser ($\lambda = 632.8$ nm) was attenuated using some neutral density filters and controlled through a half-wave plate and a Glan-Thompson cube polarizer. This system allowed to fine tune the optical power down to few picowatts. The laser beam was sent - depending on the position of a flipping mirror - either on the active area of the SiPM under test or on a reference PMT (Hamamatsu R928), previously calibrated and used to estimate the optical power incident on the SiPM. The latter was biased using a stabilized power supply and a SMD resistor (50 Ω, sensing resistor), connected between the cathode and the ground.

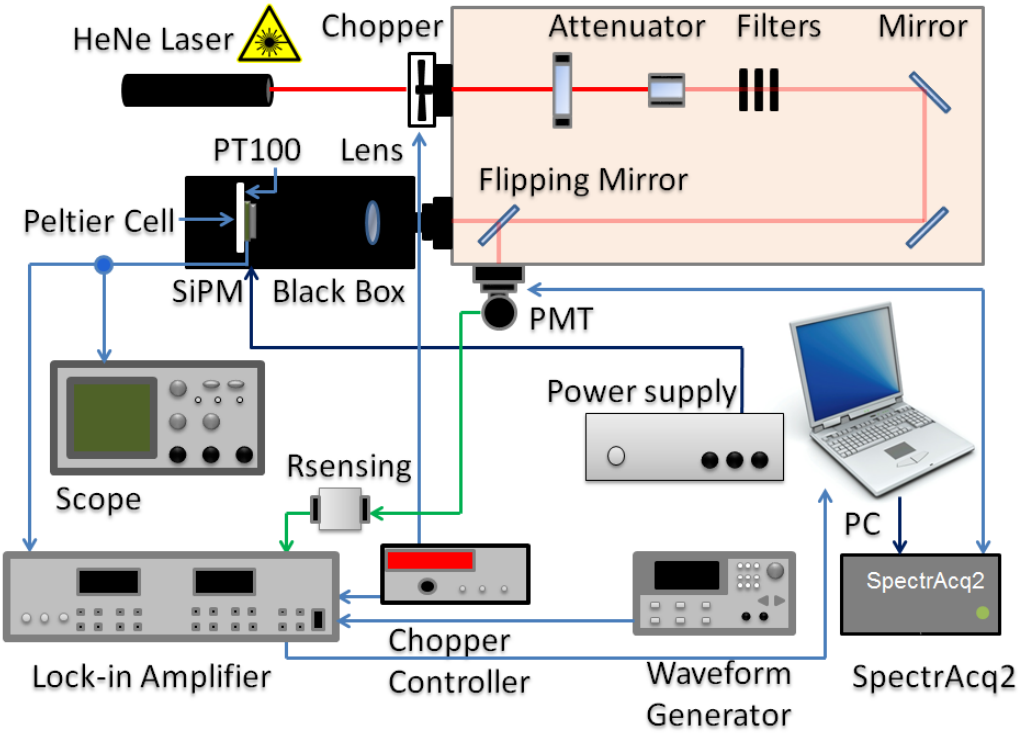

FIGURE 3.1: Sketch of the experimental setup for measurements of the SiPM SNR as a function of the applied bias, of the reference frequency and of the temperature of the SiPM package and performed in the CW regime.

The SiPM and the biasing circuit were located in a metal black box, being thus shielded by ambient light and electromagnetic noise. A 25-mm focal length lens was placed between the flipping mirror and the SiPM, making sure that the light spot covered the whole active area of the device. During measurements, the temperature of the SiPM package was controlled through a Peltier cell placed in the back side of the device and

a PT100 thermistor, placed on the Peltier cell, allowed us to record the temperature of the SiPM package. To perform low optical power measurements, a lock-in amplifier was connected to both the SiPM and the PMT outputs, while a readout system (SpectrAcq2) digitalized the signal and allowed data acquisition.

SiPM SNR is given by the ratio of the SiPM current and the rms deviation of the same current. I employed a lock-in amplifier and an optical chopper system (working at a frequency of 183 Hz) in order to acquire the average SiPM current after noise removal. The rms deviation was obtained with the lock-in amplifier set in the "noise" mode. In my measurements, I employed a 10 Hz equivalent noise bandwidth, around the lock-in amplifier reference frequency, the latter supplied by an Agilent 33220A waveform generator. The measured noise takes into account only the shot noise, resulting from the photocurrent and the dark current, while background light is not present in my setup because adequately shielded. Measurements were performed with a constant incident optical power of 11 pW, to be sure the SiPM behavior was linear up to, at least, 35.3 V [37, 48, 49].

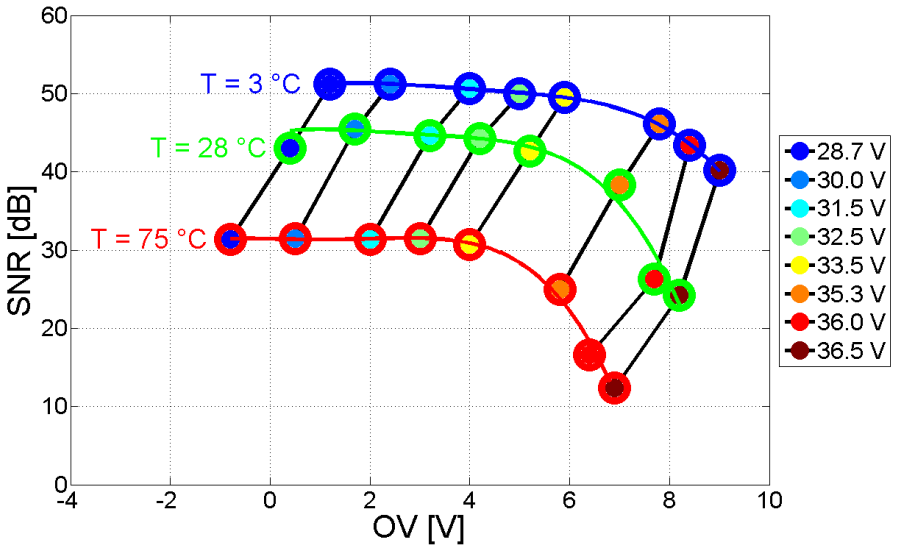

FIGURE 3.2: SiPM SNR versus applied overvoltage at $\lambda = 632.8$ nm, lock-in amplifier reference frequency of 100 kHz and at three different temperatures (3, 28, 75°C) of the SiPM package. The legend shows the applied reverse bias voltages. Blue, green and red outer circles indicate measurements performed at the temperature of 3, 28 and 75°C respectively.

Fig. 3.2 shows the SiPM SNR versus the applied overvoltage at $\lambda = 632.8$ nm and at three different temperatures (3, 28, 75 °C) of the SiPM package. The legend shows the applied reverse bias voltages between the anode and the cathode of the device. Each 3-points curve is characterized by the same bias voltage, while the applied overvoltage (OV) has been estimated taking account of the breakdown voltage (28.0 V at room

temperature) shift with temperature. The same figure exhibits a quasi-flat trend up to an OV of about 5 V. At higher OVs, I observe the SNR decrease, mainly due to the strong increase of the shot noise.

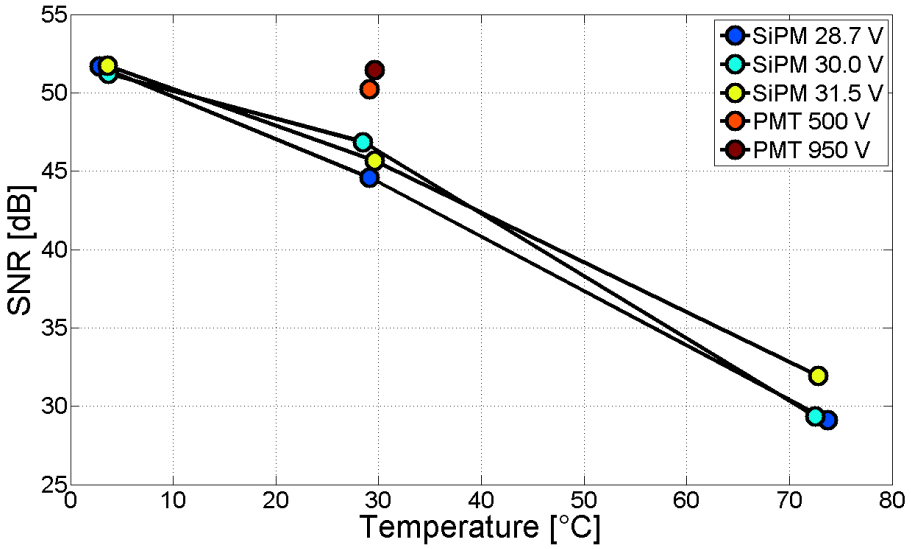

FIGURE 3.3: SiPM SNR versus temperature of the SiPM package. SNR measurements performed on the reference PMT at room temperature are plotted to make a comparison. The legend shows the applied bias voltages. These results are constant in the considered frequency range (1 - 100 kHz).

Fig. 3.3 depicts the SiPM SNR as a function of the temperature of its package and at different bias voltages. In the case of room temperature, I also compared SiPM SNR with PMT SNR. SiPM performance are outstanding, since its SNR is only ≈ 5 dB below the PMT SNR, at the same temperature. Moreover, cooling the SiPM package, by means of a Peltier cell, at a temperature of 3 °C, it reaches the PMT SNR values. This result is achieved biasing the SiPM up to 31.5 V against a bias up to 950 V for the PMT. Finally, I repeated the measurements at different lock-in amplifier reference frequencies in the range 1 - 100 kHz. I found the same results shown above and, therefore, I can conclude that SiPM SNR is constant in the explored frequency range.

Results have been compared with the theoretical law in Eq. 3.1 [51]. This expression correlates the output shot noise current I_S with the overall output current I_O, where e is the electron charge, F is the Excess Noise Factor of the SiPM ($F \approx 1$, provided by STMicroelectronics) or the Noise Figure of the PMT ($F \approx 1.3$, provided by Hamamatsu Photonics), B is the frequency bandwidth of the noise measurement system ($B = 10$ Hz) and μ is the gain of the SiPM (provided by STMicroelectronics) or the PMT (provided by Hamamatsu Photonics). The comparison between the experimental data and the theoretical values showed good agreement, therefore I could infer that the measured output noise current is actually the output shot noise current I_S.

$$I_S = \sqrt{2eI_O FB\mu} \tag{3.1}$$

Measurements of SiPM and PMT dark currents have also been performed employing an Agilent 34401A multimeter (sensitivity of the whole setup down to 0.15 nA). The SiPM exhibited an ascending trend with the reverse bias, as previously reported in section 2.3.1 (Fig. 2.3), reaching values up to a few milliamperes at the highest voltage (36 V), while the PMT output was negligible at all the applied biases (up to 950 V). However, the SiPM output dark offset, unlike the shot noise output, can be eliminated through external DC offset removal circuits.

3.3 Conclusions

In this chapter, I investigated the SNR, in CW regime, of a novel 3600 channels SiPM fabricated on a silicon p-type substrate. In particular, I showed, for the first time, my SiPM SNR measurements as a function of the applied bias, of the reference frequency and of the temperature of the SiPM package. Similar measurements were also performed on a PMT, in order to make a comparison. A 10 Hz equivalent noise bandwidth was employed, around the lock-in amplifier reference frequency.

I have found that the SNR is independent from frequency in the evaluated range 1 - 100 kHz. My results highlight the outstanding performance of this class of SiPMs, even without the need of any cooling system. Indeed, their SNR is only ≈ 5 dB below the PMT SNR at room temperature. Furthermore, cooling the SiPM package at a temperature of the Peltier cell of 3 °C, it reaches the PMT SNR values at room temperature, even if the SiPM is biased in the range of 28.7 - 33.5 V, against a bias value up to 950 V of the PMT. A physical interpretation of the results was also provided.

Chapter 4

A SiPM Application: The Optical Characterization of Infiltrated Opals for Ethanol Vapor Sensing

4.1 Introduction

In this Chapter, an innovative application of the SiPM is reported: an optical characterization of a class of photonic crystals (PCs) infiltrated with an innovative stimuli-responsive hydrogel employing the SiPM as a reference photodetector. The Hydrogel based PCs under investigation have been developed by the research group of the Prof. Clelia Dispenza of the Department of Chemical, Industrial, Computer, Mechanical Engineering (DICGIM) of the University of Palermo. After a brief summary (section 4.2) regarding the fabrication process, I will describe the measurements performed on the bare opals and on the infiltrated opals, providing physical explanations of my results (section 4.3).

At the beginning, I performed transmission measurements on bare opals in function of their position and of the incident angle, in order to test the quality and uniformity of the fabricated template.

Subsequently, I carried out optical transmission measurements on the hydrogel-infiltrated opals. Similarly to the bare opals, measurements at varying positions and angles of incidence were taken.

Finally, I a series of measurements have been performed to test the potential of the infiltrated opal as active material for ethanol vapor sensing and to determine its sensitivity.

4.2 The Fabrication of the Photonics Crystals

The PCs were obtained through the vertical deposition method (the most widely used), that, although is a relatively slow process (1-2 days to complete), provides the highest optical quality. It is based on the evaporation of the liquid forcing the spheres to arrange in the meniscus formed between a vertical substrate, the suspension and the air. The main advantages of this method are a precise control over the thickness and a superior crystalline quality of the structures. Despite the fact that this approach is affected by concentration gradients, which can lead to disturbances of the structures (e.g. growth defects and disordered domains), it has the advantage to be very simple and straightforward and it yields to significant portions of the casted film with fairly regularly packed nanoparticles [53]. The vertical deposition method was selected among the various possible techniques for the purpose of this first exploratory study, in order to obtain the highest optical quality for the fabricated PCs.

In order to fabricate the infiltrated opals, a two-step process was followed. We first obtained a crystalline colloidal array through self-assembly of monodisperse polystyrene nanoparticles to form a face centered cubic (fcc) lattice (i.e., bare opal). The final bare opal, depicted in Fig. 4.1, is 1 cm large and 1.2 cm long, while its thickness is about 650 nm. Fig. 4.2 displays a scanning electron micrograph of the fabricated bare opal, showing the good homogeneity and regularity of the structure.

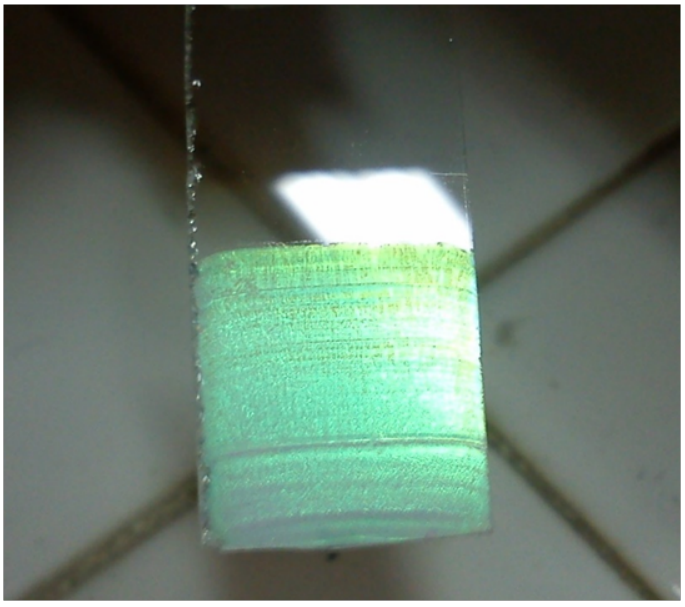

FIGURE 4.1: Photograph of the fabricated bare opal.

The obtained bare opal was subsequently infiltrated with the ethanol-responsive hydrogel precursors and the latter were then crosslinked via UV photo-polymerization. The

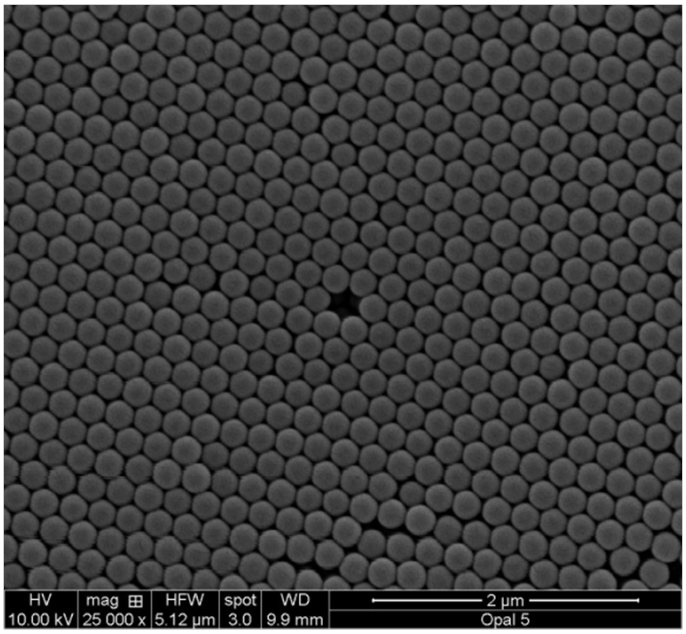

FIGURE 4.2: Scanning electron microphotograph of the periodic structure of the sample.

infiltration process of the hydrogel was followed by the color change of the deposit from white to colorless. When infiltration was completed, a quartz slide was placed on top of the deposit to reduce uncontrolled accumulation of material on the surface and to limit water loss during photo-polymerization. Irradiation was carried out using a UV irradiator, equipped with a high-pressure Hg lamp. The temperature inside the chamber was controlled during the process. After photo-curing, a thermal post-curing treatment was carried out in an oven. After removal of the topcover, samples were equilibrated in bidistilled water at room temperature. Details about the fabrication are extensively explained in [43, 54].

4.3 Experimental results and data analysis

In order to perform the optical characterization of the samples, the set-up depicted in Fig. 4.3 was used. The white light coming from a Xenon lamp was spectrally filtered by a monochromator (Horiba Jobin Yvon FHR 1000) and focused onto the opal through a 50 mm focal length lens. The monochromator possesses a spectral resolution of 0.008 nm when the slits width is set to 10 μm. Optical transmission measurements were performed in the 400-700 nm range with a wavelength step of 1 nm, dividing the transmitted power by the incident one.

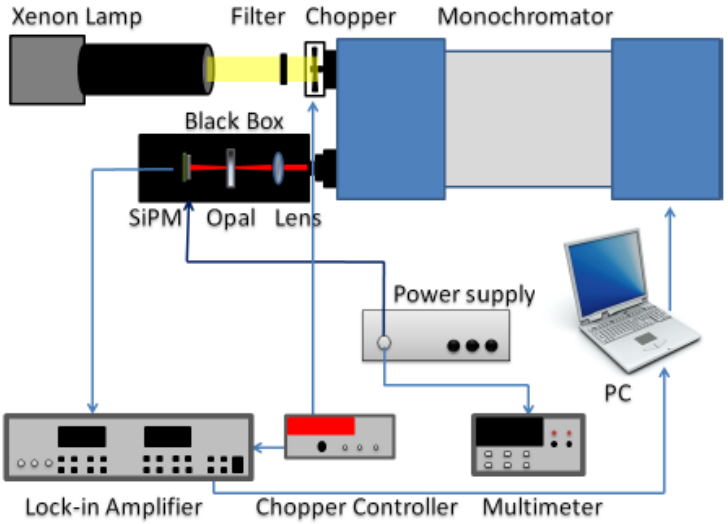

FIGURE 4.3: Sketch of the experimental setup for measurements of opal transmission spectra.

A N-on-P SiPM (described in chapters 2 and 3) [37] was used as a detector and it was connected to a lockin amplifier that, together with a chopper, helped to reduce noise. The sample, the lens and the SiPM were enclosed in a black box during the measurements, in order to isolate the detection stage from external light and electromagnetic noise.

The choice of the SiPM was due to different reasons. First of all, its outstanding performances in terms of high gain and responsivity were necessary. Indeed, transmission measurements involved very low light intensities, always inside its range of linearity (see section 2.3.2). Furthermore, the area of the light beam was smaller than the active area of the device and always impinged inside it. Finally, if compared to PMTs and APDs, the SiPM exhibits the advantages discussed in section 1.5.

To obtain the optical characterization of the infiltrated opals at different ethanol vapor concentrations, the basic set-up was modified as follows. A 100 cm^3 sealed polyethylene box, possessing two fused silica windows (to allow the passage of light) and a small hole, connected to the outside through a hose (to introduce liquids), was placed inside the metallic black box, between the lens and the SiPM (Fig. 4.4).

The sample was positioned inside the box, hung from its top, so that transmission measurements could be performed while the sample was exposed to a controlled vapor atmosphere created by a layer of liquid, filling the bottom of the box. Particular care was taken to avoid any contact between the sample and the liquid phase. The temperature of the black box was monitored by a PT100 thermistor, to ensure that it was constant during all the measurements.

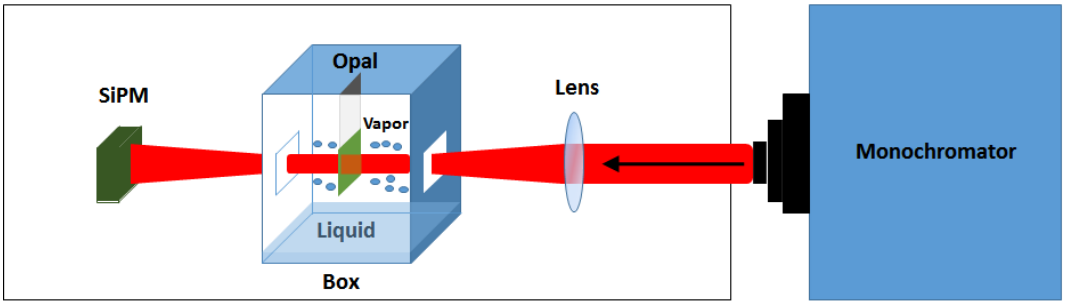

FIGURE 4.4: Sketch of the black box for measurements of opal transmission spectra.

4.3.1 Measurements performed on the bare opals

In order to test the quality and uniformity of the fabricated template, transmission measurements on bare opals, in function of their position and of the incident angle, were performed.

The chosen fabrication process provides a good uniformity on the horizontal axis (Fig. 4.1). On the contrary, due to the progressive modification of nanoparticles dispersion concentration upon solvent evaporation, there may be variations in the quality of the deposited film along the vertical axis. For this reason, a first series of transmission measurements was performed at normal incidence by varying the vertical position from the top edge of the opal (first deposited part), with a step of 0.5 mm. For each measured transmission spectrum, the Bragg peak wavelength, the Full Width at Half Maximum (FWHM) and the depth of the gap were estimated. It was observed that the Bragg resonance was centered around 508 nm ($\pm$ 3 nm) for each position. Small variations also occurred on the FWHM (42 $\pm$ 6 nm) and depth of the gap. From these results, it can be claimed that the sample shows a good homogeneity and exhibits its best optical properties (i.e., smaller FWHM and deeper gap) in the first deposited layers of the fabricated bare opal, as it would be expected, being only minimally affected by changes in dispersion concentration upon solvent evaporation.

Subsequently, a second series of measurements was carried out in correspondence of the vertical opal position that showed the best optical properties, by varying the angle of incidence (from 4° to 41.5°). These measurements have a double goal: they represent a further test on the optical quality of the opal, and they also provide an indirect measurement of the PS sphere diameter. The latter is an important parameter, useful to achieve the effective index of the infiltrated opal.

The results are shown in Fig. 4.5: at increasing angles of incidence, the Bragg peak is blue-shifted, from $\lambda_B = 510$ nm at $\Theta = 4°$ to $\lambda_B = 457$ nm at $\Theta = 41.5°$. It is worth noticing that, at angles greater than 40°, a change in the shape in the spectrum can be

observed. This is related to the interplay of the stop band and of the excitation of the photonic modes observed in the density of states, which takes place for large angles of incidence [55]. Moreover, scattering becomes relevant, causing a strong reduction of the transmitted light intensity.

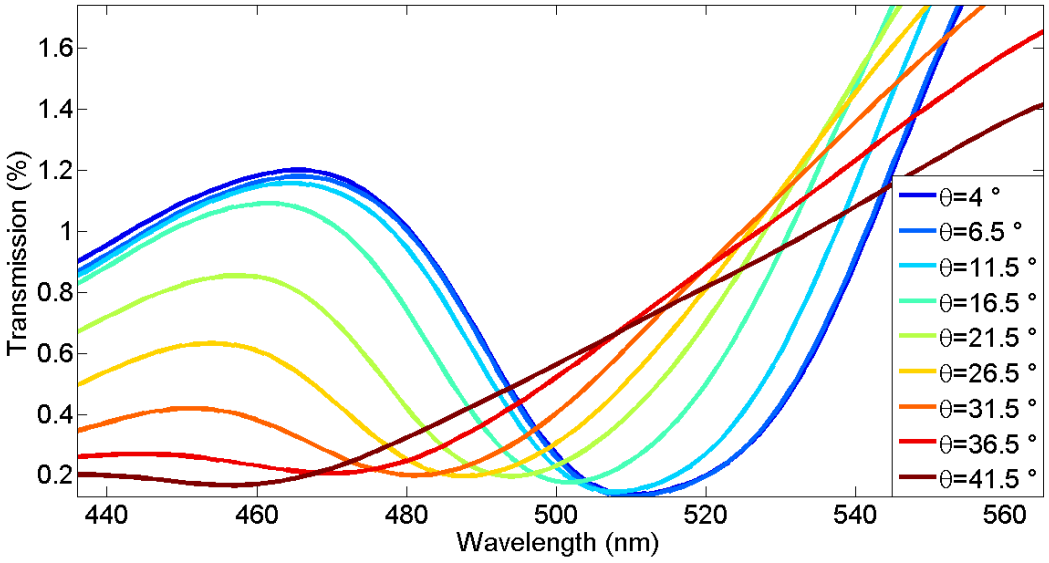

FIGURE 4.5: Transmission spectra of the bare opal at varying angles.

Measurements are in good agreement with the theoretical behavior of PCs. In fact, as known, because of the Bragg diffraction, the transmission spectrum of an opal presents a minimum peak, whose position is described by the general relation that combines Snell's and Bragg's laws. More details are available in [43, 54, 56–59].

My experimental data were compared with the theoretical position of the Bragg wavelength, using the sphere diameter as the only fit parameter (see Fig. 4.6) [43]. The best fit value for the diameter of the nanoparticles is 213 nm, that falls within the range provided by the nanoparticles supplier.

As it can be seen, the agreement between the theoretical curve and the experimental data is very good. Error bars in figure (about 2 nm) are mainly due to the spectral resolution of the monochromator, since, in order to have enough optical power, its slits aperture was set to 1 mm.

4.3.2 Measurements performed on the infiltrated opals

I carried out optical transmission measurements, on the hydrogel-infiltrated opals, on samples equilibrated in air at a temperature of 23.8 °C and relative humidity of 45% for minimum 24 h. In order to verify that the infiltration process did not alter the periodic

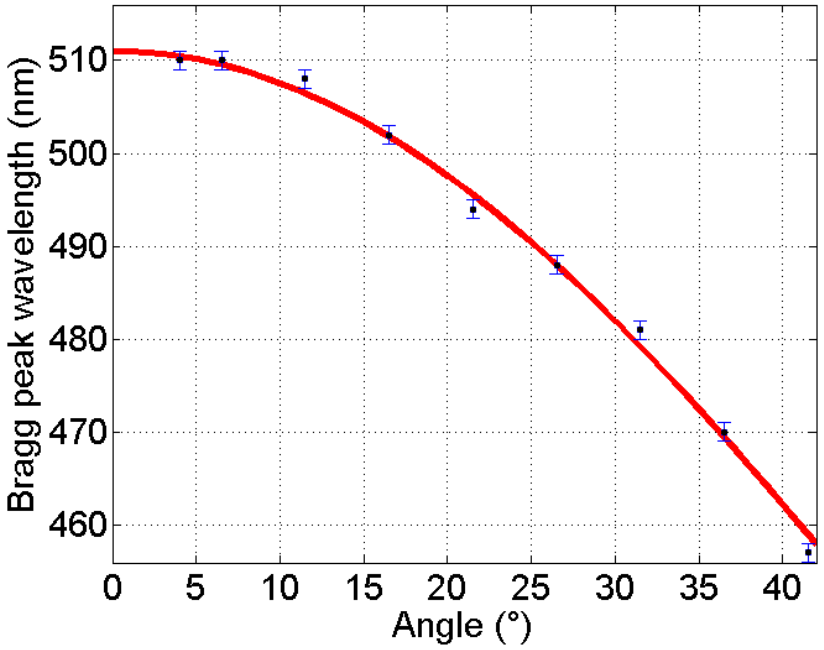

FIGURE 4.6: Bragg peak wavelength versus angle of incidence: theoretical values (red curve) and experimental data (black circles). Blue lines are the error bars (± 1 nm).

structure of the bare opal, I performed measurements at varying vertical positions and angles of incidence. The Bragg resonance at normal incidence was now centered at 548 (± 6) nm, with a red-shift of 40 nm with respect to the bare opal. The performed measurements at varying vertical positions (here not shown) indicate that the periodic structure was preserved with a fairly good uniformity. Similarly to the bare opal, in correspondence to the position that showed the best optical properties (again in the first deposited layers near to the up edge of the fabricated opal), measurements at varying angles of incidence were taken. Bragg peak is blue-shifted at the increase of the angle of incidence, in accordance to the general relation that combines Snell's and Bragg's laws [43], similarly to the direct bare opal. Parallel measurements and calculations performed by other members of the research group through a fully-automated refractometer (Metricon Model 2010/M Prism Coupler), allowed to obtain accurate values of the refractive index and of the filling factor [60] for the infiltrated opal (respectively, 1.513 and 0.225), as described in [43, 54].

Subsequently, I executed a series of measurements to test the potential of the infiltrated opal as active material for ethanol vapor sensing.

The hydrogel used to infiltrate the bare opals is expectedly swollen by water, retaining some hydration when exposed to the air, but - more interestingly - it is further swollen when exposed to ethanol vapor. This property is especially interesting in view of the

potential application of this sensing material in breathalyzers, where water vapor is one of the main components of the analyte, in addition to ethanol and a number of others components present in lower concentrations. For this reason, in order to analyze the optical response of the infiltrated opal at varying concentrations of ethanol vapor, it is of outmost importance to first study its behavior in the presence of water vapor.

The sample, in equilibrium with air at a temperature of 23.8 °C and relative humidity of 45%, was placed within the sealed box. Then, distilled water was inserted into the box through the hose and transmission measurements were taken at normal incidence, approximately every 10 minutes. During the whole process, the temperature inside the black box was continuously measured, resulting approximately constant (about 24 °C).

In the chosen experimental conditions, the time required for establishing the liquid-vapor equilibrium inside the small box is expectedly much lower than the time required for the sample to reach the equilibrium swelling conditions in the new environment. Therefore, vapor phase composition changes can be neglected. As shown by the transmission spectra depicted in Fig. 4.7, the Bragg peak wavelength was red-shifted (from 543 nm at t = 0 min to 576 nm at t = 220 min), while the transmittance decreased. After 220-250 minutes, there were no more significant variations of the spectra, so it can be assumed that the infiltrated hydrogel reached its equilibrium swelling condition. The increase of the Bragg peak wavelength as a function of the time (Fig. 4.8) can be explained by the progressive increase of the relative distance among polystyrene beads in the periodic structure of the infiltrated opal, as a result of further swelling of the hydrogel in the watervapor saturated atmosphere.

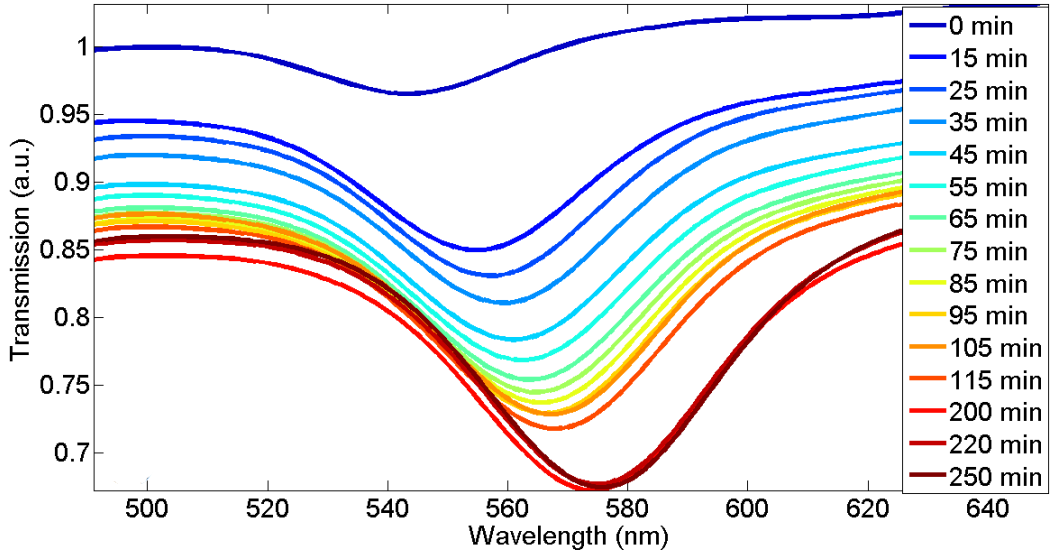

FIGURE 4.7: Response of the opal to water vapor: transmission spectra.

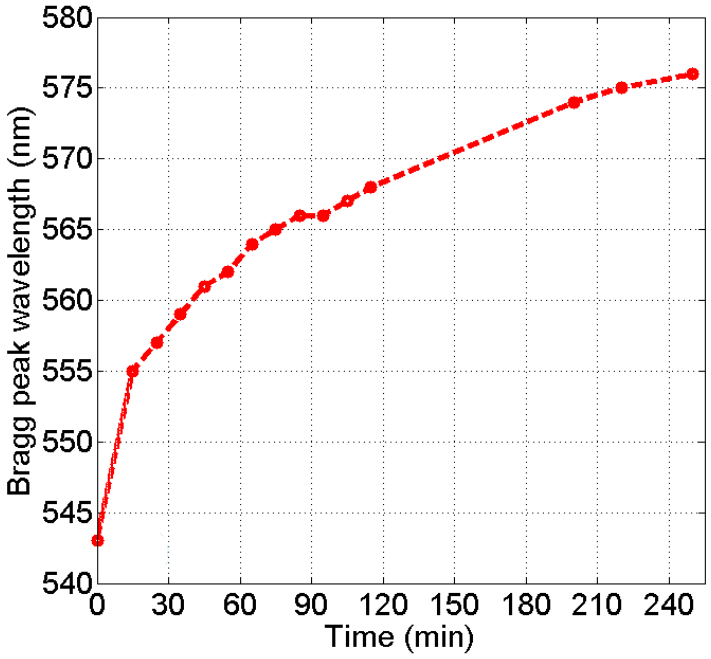

FIGURE 4.8: Response of the opal to water vapor: Bragg peak wavelength versus time.

By using the above-mentioned refractometer, other members of the group measured the refractive index of the hydrogel exposed to water vapor, obtaining the value of 1.468 for the refractive index. Therefore, the latter decreases when the hydrogel absorbs water vapor. This leads to a dielectric contrast increase for the photonic crystal (being the refractive index of the polystyrene independent on the water concentration). As known [61, 62], both the FWHM of the stop band and the peak depth increase with higher dielectric contrasts, thus explaining the behavior of the curves in Fig. 4.7.

In addition, an overall decrease of the transmission is observed, even far from the stop band. This can be explained as follows: the infiltrated opal maintains an unwanted, although very thin, layer of non-structured hydrogel on its surface. When exposing the sample to water vapor, the hydrogel noteworthy increases its surface roughness, which produces a stronger light scattering. The latter, together with the finite area of the employed photodetector, explains the trend shown in Fig. 4.7.

The transmission spectrum of the water-saturated infiltrated opal was used as a reference for subsequent measurements carried out in the presence of both water and ethanol vapors.

Liquid ethanol was progressively added to water into the bottom of the box. At any step of addition, a new series of transmission measurements was taken, approximately every 10 minutes, until the new equilibrium swelling condition for the sample was reached. This procedure was repeated four times at gradually increasing values of ethanol concentration

Liquid phase (vol:vol)	***EtOH* in the vapor phase (mole fraction)**	***H_2O* in the vapor phase (mole fraction)**	**EtOH in the vapor phase (ppm)**	**Measured Bragg peak wavelength (nm)**
1:9	9.6×10^{-3}	0.0300	15220	611
2:9	16.3×10^{-3}	0.0295	26000	638
3:9	21.0×10^{-3}	0.0289	33360	656
4:9	24.7×10^{-3}	0.0284	39033	669

TABLE 4.1: Conditions of the optical transmission measurements on the hydrogel-infiltrated opals.

in water (for each solution I reset the initial time, t = 0 min). Measurement conditions are summarized in Tab. 4.1.

Figs. 4.9 and 4.10 display the transmission spectra at the mole fraction of 9.61×10^{-3} taken at different time intervals after the addition of ethanol. It can be observed the following:

1. An initial significant decrease of the transmittance curve, which is partially restored with time.
2. A progressive increase of the Bragg peak band depth.
3. A concomitant red-shift of the band.

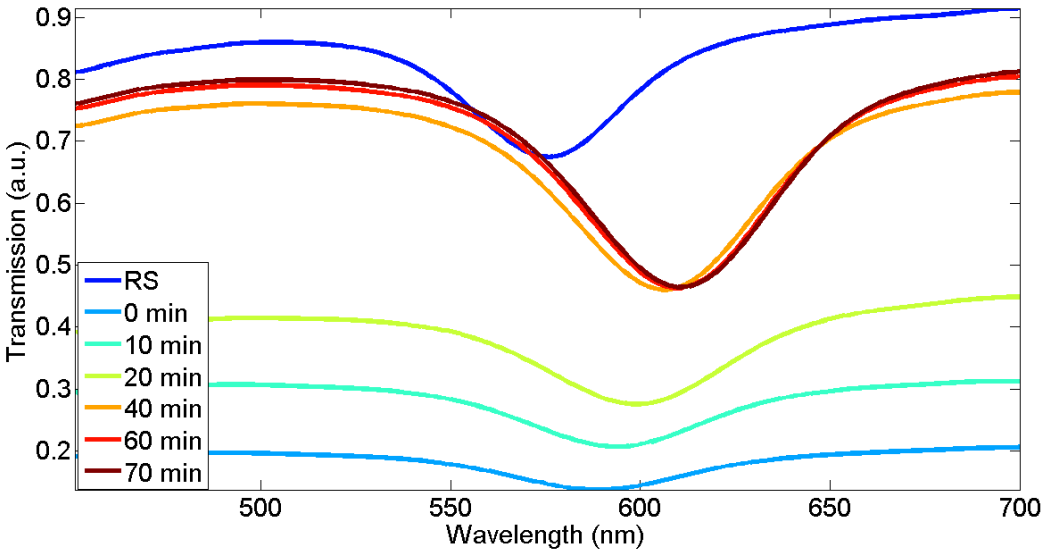

FIGURE 4.9: Transmission spectra at a mole fraction of 9.6×10^{-3}. RS in the legend stands for reference spectrum, corresponding to the water-saturated opal.

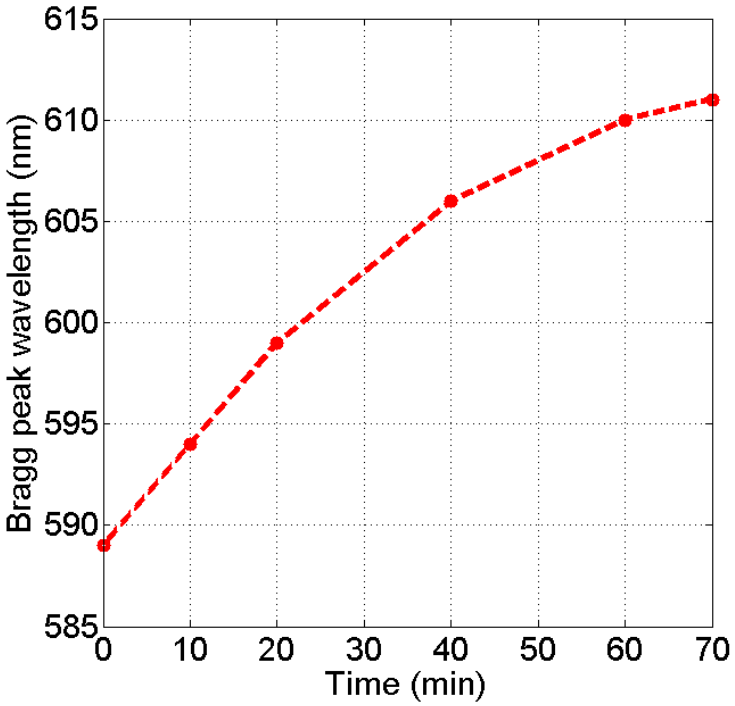

FIGURE 4.10: Bragg peak wavelength versus time at a mole fraction of 9.6×10^{-3}.

The reduction in transmittance, also in this case, is due to an increase of the roughness of the thin hydrogel layer present on the opal surface, when the sample is exposed to ethanol vapor. The main difference, if compared to the case of water vapor exposition, is that such a roughness disappears in less time, thus explaining the partial recovery of transmittance in Fig. 4.9. Simultaneously, the Bragg peak shifts toward higher wavelengths, due to the further swelling of the interstitial hydrogel operated by the absorbed ethanol, which progressively increases the distance between the embedded polystyrene beads and the depth of the infiltrated opal swollen by the ethanol/water mixture. In Fig. 4.10 the Bragg peak wavelength shift as a function of the time is shown: it can be noticed that a steady-state condition is approached after approximately 1 hour.

The response time (τ_{90}) of the sensor, determined according to the definition of τ_{90} given in [63, 64] (i.e., the time that it takes the sensor to reach 90% of its steady-state value after the introduction of the analyte), was measured when passing from a condition of equilibrium with water-vapor saturated air to an atmosphere constituted by air/water/ethanol at 9.61×10^{-3} mole fraction of ethanol. A response time of about 47 minutes was obtained. This is quite high, but it should be considered that it actually refers to the response of a hydrogel infiltrated in the interstitial spaces of a polystyrene photonic crystal, which is indeed impermeable to ethanol. Therefore, the attainment of the steady-state conditions requires sorption and diffusion of the analyte through the confined hydrogel and the cooperative dynamic rearrangements of the macromolecular

segments between crosslinks of the latter. The removal of the polystyrene template is expected to lead to significant reductions in response time.

For the other concentrations a similar trend is observed: the Bragg peak wavelength increases with time because of the further swelling of the hydrogel at the increase of ethanol concentration, while the transmission at the Bragg wavelength first strongly drops down, then it is partially recovered.

Fig. 4.11 summarizes the Bragg wavelength shift versus time for the four different analyzed mole fractions. It is worth noticing that the Bragg peak wavelength increases not only with time for each concentration, but also with the concentration of ethanol in the vapor phase.

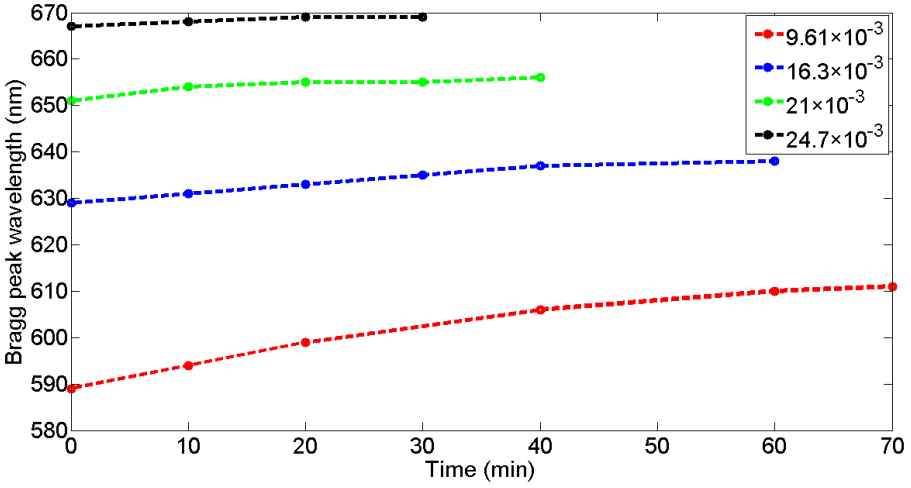

FIGURE 4.11: Bragg peak wavelength of the infiltrated opal versus time at varying mole fractions.

The behavior of the structure based on the infiltrated opal is now described by comparing the steady values obtained during the different measurements. In particular, transmission curves at the steady state and at varying mole fractions are depicted in Fig. 4.12. The Bragg peak is shifted towards higher wavelengths at the increase of ethanol mole fraction in the vapor phase, thus proving the potential of the infiltrated opal as active material for ethanol vapor sensing. In detail, as shown in Fig. 4.13, the Bragg peak wavelength is shifted, almost linearly, from 576 nm (water-saturated opal) to 669 nm (mole fraction $= 24.7 \times 10^{-3}$), in a wide concentration range. Fig. 4.14 shows a photograph of the infiltrated opal immediately after the measurement at ethanol vapor mole fraction of 24.7×10^{-3}. A visual color change, in the PC structure, was observed from green (sample in equilibrium with air at a temperature of 23.8 °C and relative humidity of 45%, as in Fig. 4.1) to red (as in Fig. 4.14). An extensive explanation of the abovementioned wavelength shift is reported in [43, 54, 65, 66].

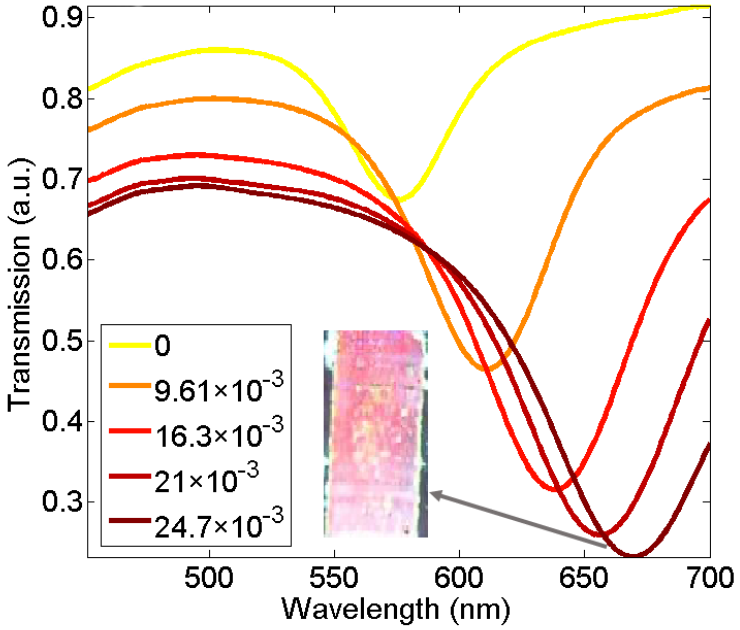

FIGURE 4.12: Transmission spectra at varying ethanol vapor concentrations after the steady value has been reached. The inset in shows a photograph of the infiltrated opal immediately after the measurement at ethanol vapor mole fraction of 24.7×10^{-3}.

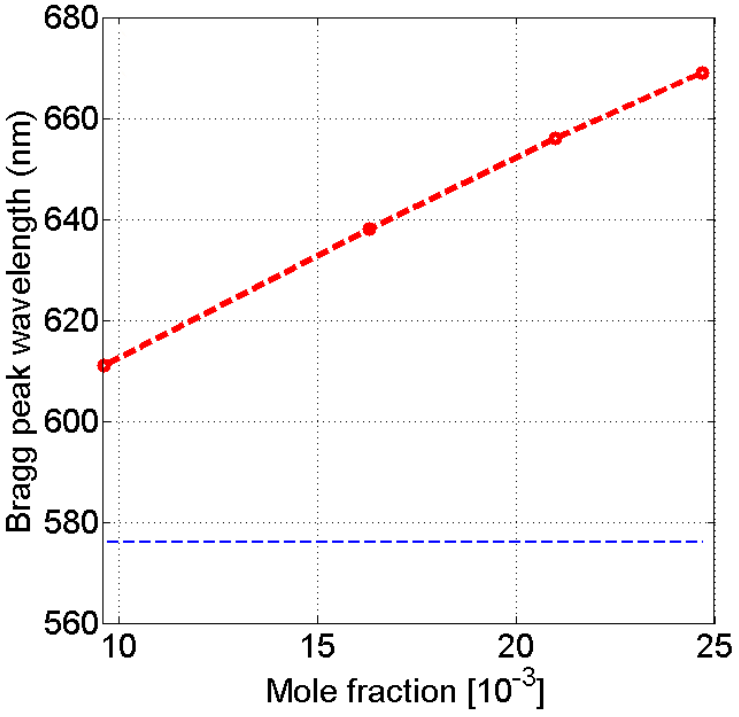

FIGURE 4.13: Bragg peak wavelength at varying ethanol vapor concentrations after the steady value has been reached. The dashed blue line is the reference, i.e., the Bragg peak wavelength for the water-saturated opal.

FIGURE 4.14: Photograph of the infiltrated opal immediately after the measurement at ethanol vapor mole fraction of 24.7×10^{-3}.

Finally, the sensitivity of the infiltrated opal was determined. As known, the sensitivity of a sensor can be defined as the change of its output with respect to the input (i.e., the measured quantity) [67]. In this case, I can define the sensitivity as the ratio of the variation of the Bragg peak wavelength and the variation of the ethanol vapor mole fraction. As previously discussed, the Bragg peak wavelength is shifted almost linearly at increasing ethanol vapor mole fractions. Therefore, by means of a linear interpolation of the experimental data in Fig. 4.13, I found a value of sensitivity (i.e., the slope of the measured data) equal to 3799.2 nm/mole fraction, or, equivalently, 2.3983×10^{-3} nm/ppm. This value is not too far from what found in literature for other chemical sensors [68, 69] and from other ethanol vapor sensors [70, 71]. The response of this photonic crystal presents a range of linearity (more than 20000 ppm) at high values of ethanol concentrations. I also qualitatively compared my results with those reported in [72, 73], where the behavior of photonic crystal structures with liquid ethanol (not ethanol vapor) has been studied. In particular, I found that my wavelength shift is linear and comparable to that reported in [73], while it is smaller than in [72], even though in [72] the shift is not linear. The described processes (change in dielectric contrast, swelling and Bragg shift) are reversible. In fact, transmission spectra obtained after water and ethanol evaporation, drying and re-equilibration in air provided the same curves shown by the original opal. The time required by the structure to reach the normal base line after exposure to ethanol vapor was measured and it resulted to be less than 1 minute.

4.4 Conclusions

In this chapter, I presented an optical characterization of a novel class of materials based on polystyrene opals infiltrated with an innovative stimuli-responsive hydrogel, employing the SiPM as a reference photodetector. The chemical composition of the hydrogel network was specifically engineered to be able to show significant swelling when exposed to ethanol vapor. The above-mentioned hydrogel also swells in the presence of water, retaining some hydration when exposed to the air, and maintains its optical and mechanical properties after repeated cycles of swelling and deswelling, by alternate exposition to ethanol vaporsaturated and ethanol vapor-free atmospheres. These properties make this hydrogel an ideal sensing material to be applied into inexpensive and minimally invasive breathalyzers.

The optical characterization of the hydrogel-infiltrated opals shows that, at increasing mole fractions of ethanol vapor, the Bragg peak wavelength is red-shifted from 576 nm (water-saturated opal) to 669 nm (ethanol mole fraction of 24.7×10^{-3}). According to these results, the fabricated nanostructured film can be used as a sensing material, with a linear behavior (more than 20000 ppm) at high values of ethanol concentrations and a good sensitivity (2.4×10^{-3} nm/ppm). As a matter of the fact, these infiltrated opals represent the first photonic crystal based structures for ethanol vapor sensing in the visible region of the spectrum: their remarkable Bragg peak shift make it possible to visually notice, through a change in the opals coloration, the variations in ethanol vapor concentration. Moreover, they present a linear optical response, at high values of concentrations, especially if compared to other kinds of already existing ethanol vapor sensors [71].

This activity, not only represents an important proof of the SiPM applications, but also shows innovative developments for the ethanol sensing.

Chapter 5

Conclusions

In this Thesis I have reported, for the first time, an extensive experimental study of two novel classes of Silicon Photomultipliers (SiPMs) performed in the continuous wave (CW) regime. These SiPMs employ N-on-P and P-on-N physical structures, the latter obtained inverting the doping of the layers of the standard N-on-P technology.

The optical comparison showed SiPM responsivity measurements as a function of the incident optical power (from hundreds of nanowatts down to sub picowatts) at different bias voltages and monitoring the temperature of the SiPM packages. These tests permitted to investigate the causes that limit the linear behavior of the devices: the finite number of photodiodes making up the device, the temperature, the dark current and the operating bias. Responsivity measurements allowed to define an innovative criterion to establish the maximum usable range of SiPM in the CW regime, estimating the maximum ratio of the output current and the applied overvoltage. Such a condition is quite close to the definition of the maximum usable range of SiPM in pulsed mode found in literature.

Furthermore, responsivity measurements have been performed on a broad spectrum, ranging from ultraviolet to near infrared (340 - 820 nm). The spectral characterization highlighted the responsivity peaks in the red and in the blue ranges for the N-on-P and the P-on-N technologies, respectively.

The characterization continued with a study of the SiPM Signal-to-Noise Ratio (SNR). In particular, I showed, for the first time, SiPM SNR measurements as a function of the applied bias, of the frequency and of the temperature of the SiPM package in the CW regime. SNR measurements were also performed on a photomultiplier tube, in order to make a comparison. The results highlight the outstanding performance of these SiPMs, even without the need of any cooling system.

Once the device was characterized, I successfully tested it in a new application. I employed the SiPM as a reference photodetector to perform an optical characterization of an innovative class of artificial opals for ethanol vapor sensing. Measurements showed that, if these opals are kept constantly moist (so they would not respond to water vapors), their transmission spectra in the visible range strongly change, from green to red, at varying concentrations of ethanol vapor. This activity, not only represented an important proof of the SiPM applications, but also exhibited innovative developments for the ethanol sensing.

In appendix, I also reported an electro-optical characterization of a novel class of 4H-SiC vertical Schottky UV detectors. In particular, I performed responsivity measurements as a function of wavelength (200 - 400 nm range), of the device package temperature and of the applied reverse bias, discussing the performances of the devices.

I believe my results will contribute to the understanding and implementation of the SiPM on the investigated CW regime. This kind of excitation is scarcely discussed in literature, even though it seems to be very useful in applications in which a huge dynamic range from sub picowatts to several nanowatts is mandatory. This outstanding feature can be exploited in very sensitive power meters and, above all, in those medical imaging systems where the detected optical power is significantly variable with the distance between the detector and the source, like in the near-infrared spectroscopy and in immunoassay tests.

Appendix A

Responsivity Measurements of SiC Schottky Photodiodes for UV Light Detection

A.1 Introduction

The desired operational characteristics of a suitable photodetector should be in principle: high responsivity, linearity of the photocurrent as a function of incident optical power, high signal-to-noise ratio and appropriate spectral selectivity. The relative weight of these different aspects depends on the intended applications. For example, in ultraviolet (UV) imaging, where real-time fast signal treatment is sought, short response times are needed.

Until recently, photomultiplier tubes (PMTs) were the preferred devices for UV light monitoring [74, 75]. However, their limitations (i.e. low quantum efficiency in the UV range, large size, high cost, high bias voltage, and fragility) have driven research towards the production of more miniaturized and reliable technology. In fact, the need for UV detection systems for portable or shipped applications has led to solutions in terms of semiconductor-based UV photodetectors, where the active devices are mainly photoconductors, p-i-n photodiodes, Metal-Semiconductor-Metal photodiodes, or Schottky junction photodiodes. The application areas that utilize UV signals have expanded in recent times and a growing interest is in the following scientific fields: laser-induced fluorescence biological-agent detection, astronomy, water sterilization, flame detection monitoring, sterilization systems, security and non-line-of-sight covert communications [74, 76–79].

The above mentioned applications represent advances made possible in recent years due to the significant progress in epitaxial growth technologies and processing of wide bandgap (and wide UV absorbing) semiconductors. Among the latter, Silicon Carbide (SiC), owing to its wide bandgaps has proved to be an attractive material for high-speed optical detection in the UV regime, demonstrating high quantum efficiency in the whole 200 nm - 400 nm UV range (with peak value between 270 and 300 nm), excellent visible blindness and low dark current, besides being robust and able to operate at high temperatures [80–84]. Furthermore, recent technological advances have allowed the production of so-called 4H-SiC UV photodetectors, which have attractive operational features. Among these are included: low dark-current, high internal quantum efficiency, excellent visible blindness, operational performance over a wide temperature range, long-term stability/resistance under UV irradiation, sensitivity to low photon fluxes and top dynamic performances [74, 77, 81, 84–86].

In this chapter I will report on the design and electro-optical comparison of three novel classes of 4H-SiC vertical Schottky UV detectors, named SiC8, SiC10 and SiC20, obtained employing Ni_2Si interdigitated strips whose pitch is 8, 10 and 20 μm, respectively. I will illustrate, in dark conditions, the forward and reverse I-V characteristics as a function of the temperature and the C-V characteristics. Responsivity measurements as a function of the wavelength, of the applied bias and of the temperature are reported and examined.

A.2 Device Structures and Fabrication

The Schottky UV photodiodes were produced at the STMicroelectronics R&D facilities on n-type 4H-SiC epitaxial layers, 4 μm thick, onto an n-type heavily doped substrate, both layers being separated by an interposing buffer layer.

The doping concentration of the epilayer was $1 \times 10^{14} cm^{-3}$ while the doping concentration of the substrate layer was $1 \times 10^{19} cm^{-3}$, as indicated by the supplier. Ohmic contacts on the sample back side were formed by sputtering of a 200 nm Ni film, followed by a rapid annealing at 1000 °C. The 2-μm-wide Ni_2Si stripes were obtained combining standard optical lithography with highly selective metal etching. A rapid thermal processing at low temperature (700 °C) was used for the formation of Ni_2Si, Schottky barrier[85]. An AlSiCu metal layer (1 μm thick) was sputtered on the top side of the device to define the pad for the anode contact by photolithography. Finally, a metallic multilayer Ti-Ni-Au (1 kÅ/5 kÅ/0.5 kÅ) was sputtered on the rear of the wafer for the cathode ohmic contact. The exposed SiC surface area was carefully maintained clean during all of the processes to the end, in some cases protected by sacrificial oxide

layers, to avoid any contamination. In Fig. A.1, a schematic cross section and optical microscope images (Figs. A.2 and A.3) of the 4H-SiC Schottky photodiode investigated in this work are reported.

Each diode shows a 0.38 × 0.38 mm^2 active area and a 2 μm Ni_2Si strip width. The distance between the Ni_2Si stripes depends on the specific class and it is 8 μm for the SiC8, 10 μm for the SiC10 and 20 μm for the SiC20 class. All these device classes provide the same package that includes seven diodes (see Figs. A.2 and A.3).

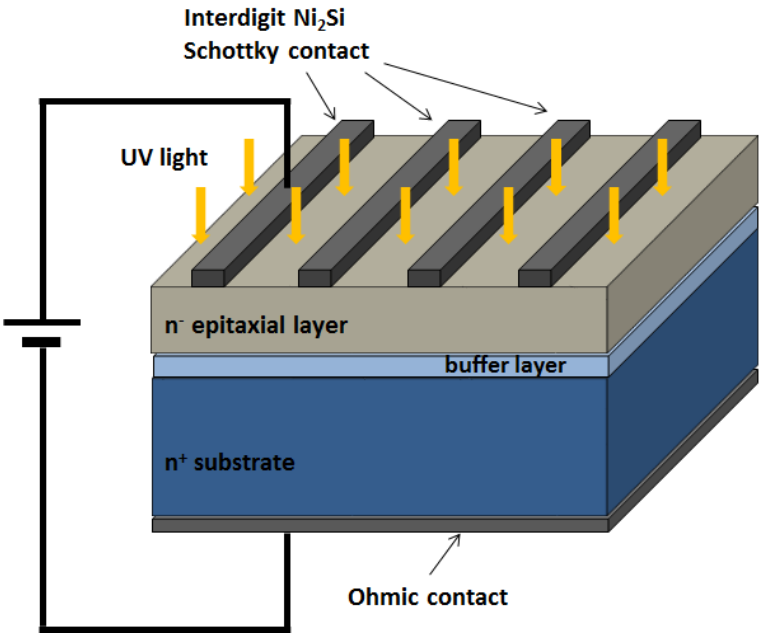

FIGURE A.1: Schematic cross section of the 4H-SiC Schottky photodiode.

A.3 Experimental Results

In this section, I summarize the first results concerning the electrical and optical characterization of the SiC photodiodes described in section A.2. In particular, forward and reverse current-voltage (I-V) and responsivity measurements, at various temperatures, have been carried out. The tests were performed post-processing, in order to have a better understanding of the optical measurements.

Undoubtedly, characterization of these photodiodes at different temperatures is one of the most important parameters, in view of the final applications of these UV-light detecting and monitoring components, also in relation to the management and reading features required of control circuits (e.g. choosing resistors with appropriate temperature).

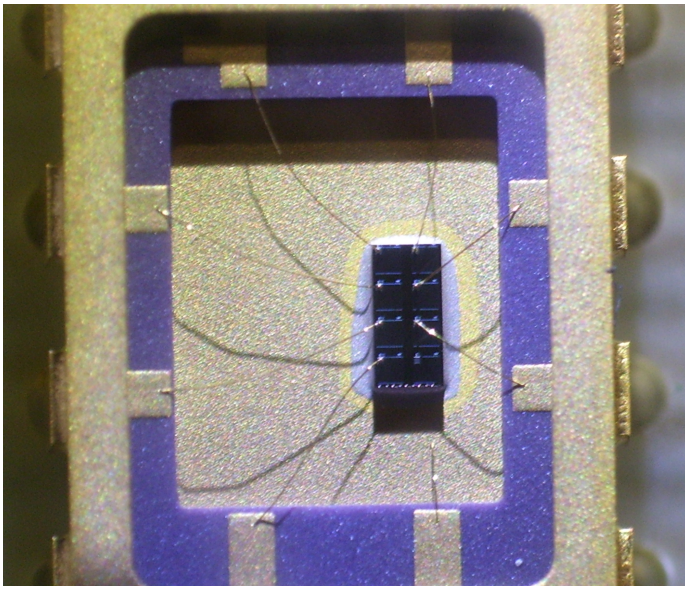

FIGURE A.2: Optical microscope image of the package of the 4H-SiC Schottky photodiode.

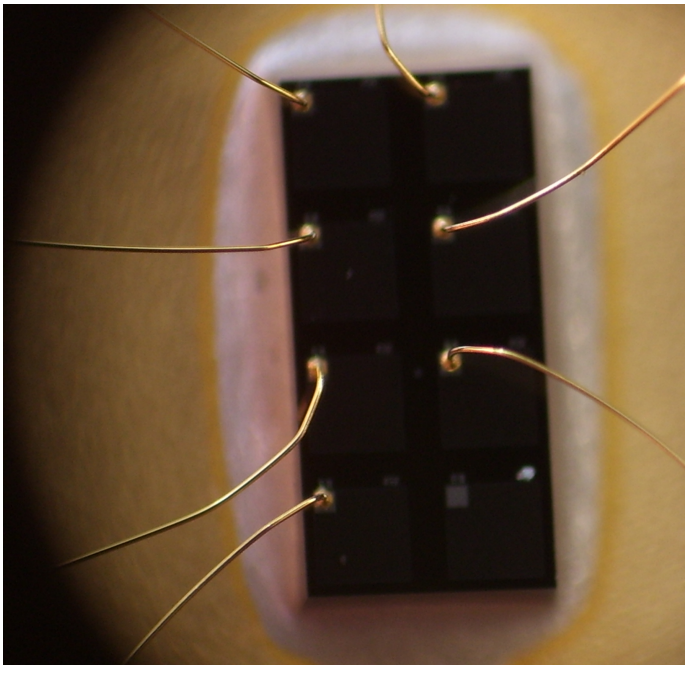

FIGURE A.3: Optical microscope image of the 4H-SiC Schottky photodiode.

A.3.1 Electrical Characterization

I performed reverse and forward current measurements at various temperatures in the -20 ÷ 110 °C range (see Figs. A.4 and A.5) on several photodiodes kept in dark condition using a temperature-controlled probe station and a semiconductor parameter analyzer (Agilent 4155C).

The semilogarithmic plot in Fig. A.4 illustrates the typical reverse current characteristics, obtained at different temperatures, for the SiC8 class devices under test. The leakage current is about 3 pA at -5V and 25 °C and remains relatively stable at higher temperatures.

Fig. A.5 shows the semilogarithmic plot of the I-V forward currents measured on the same device at the same temperatures of Fig. A.4.

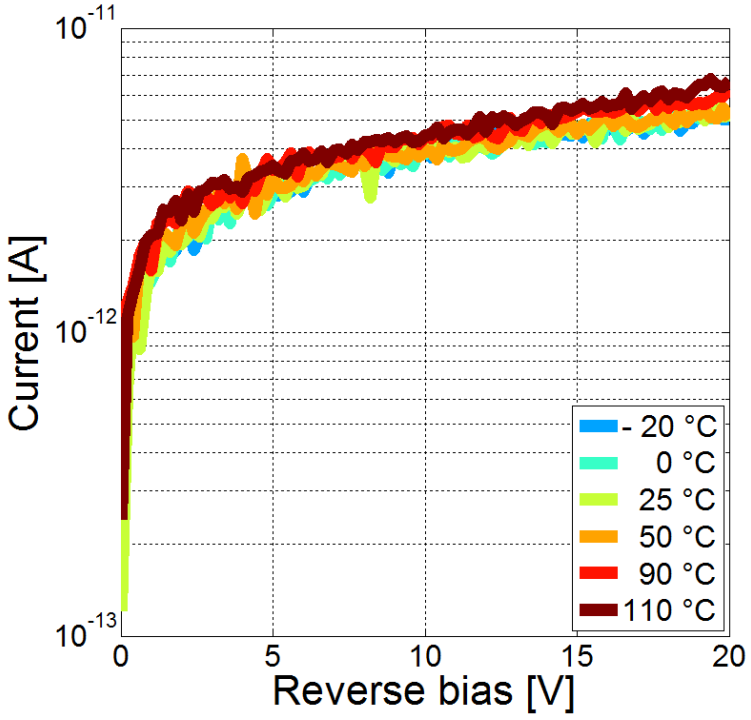

FIGURE A.4: Reverse I-V characteristics for the SiC8 class, in the range -20 - 110 °C and in dark conditions.

As expected, the increase in temperature produces a decrease of the voltage threshold due to the thermal generation of carriers. The reverse current (dark) appears to be almost constant and independent of the applied temperature. This means that the heat produced by generation centers within the energy gap of the material seems to exert negligible effects. In Fig. A.6, I illustrate the capacitance of the device measured at 100 kHz readout frequency and 25 °C as a function of the applied reverse voltage.

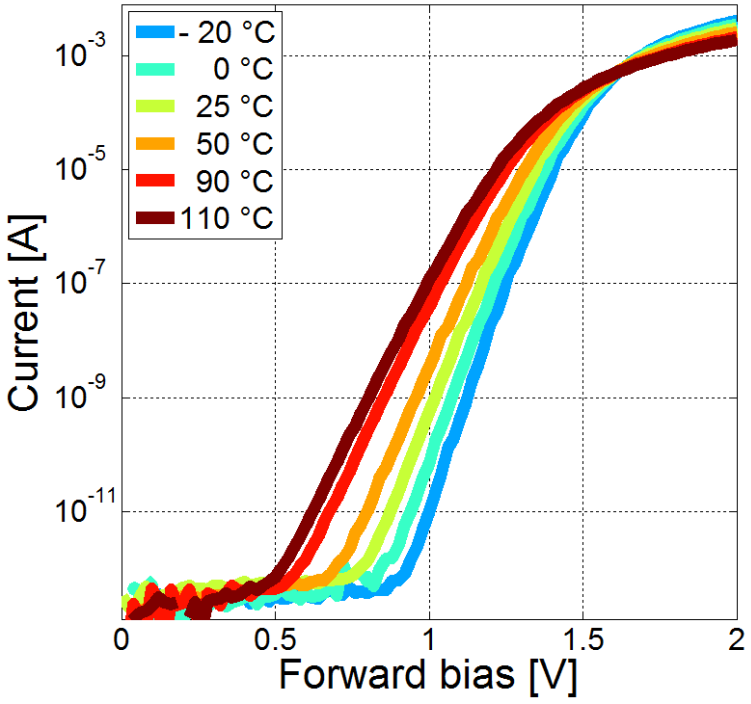

FIGURE A.5: Forward I-V characteristics for the SiC8 class, in the range -20 - 110 °C and in dark conditions.

Capacitance measurements were performed by using a precision LCR meter (Agilent 4284A). The capacitance does not decrease significantly by increasing the reverse bias applied to the device. This can be considered the first experimental evidence that contiguous depleted regions merge (surface pinch-off condition) at low reverse voltage. This effect is due to the low doping of the epilayer which allows to create wide surface-depleted regions around each Ni_2Si strip already at low reverse biases (near 0 V).

A.3.2 Optical Characterization

In order to evaluate the SiC responsivity on the UV spectrum and at different bias voltages and temperatures, I performed an optical characterization employing the setup sketched in Fig. A.7. The white light produced by a xenon lamp was spectrally filtered by a monochromator. The output monochromatic light was sent to the SiC under test or to the reference PMT, according to the position of a flipping mirror placed inside the monochromator and controlled via software. The SiC and its biasing circuit were located in a metallic black box and a lock-in amplifier was employed in order to reduce noise. The width of the monochromator slits was set at 1 mm (corresponding to a spectral resolution of about 2 nm) and I employed a 20 mm focal length lens to focus the optical beam to a waist of about 150 μm, in order to send all the optical power within the

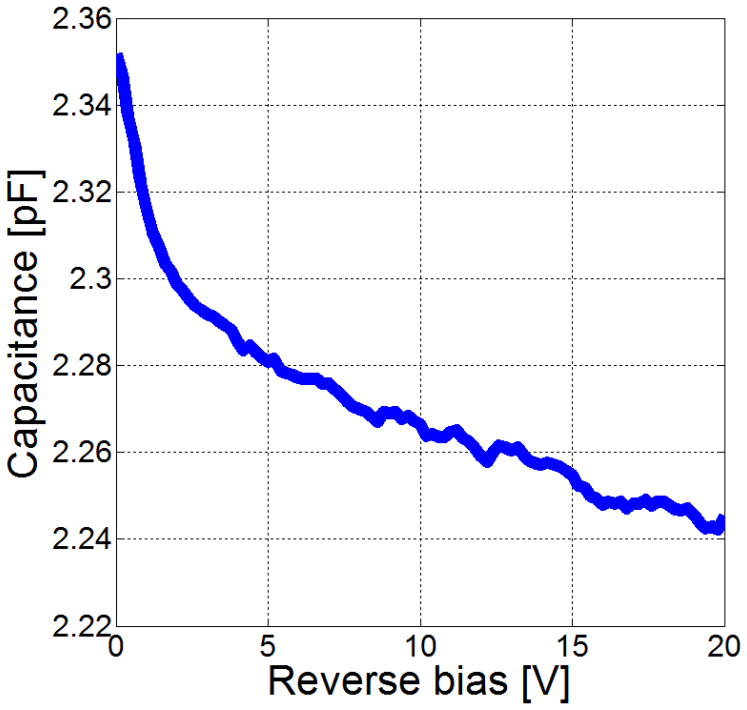

FIGURE A.6: Capacitance of the SiC8 class, measured at a readout frequency of 100 kHz and at a temperature of 25 °C as a function of the reverse bias.

sensitive area of the devices. Spectral measurements were performed within the 200 - 400 nm range.

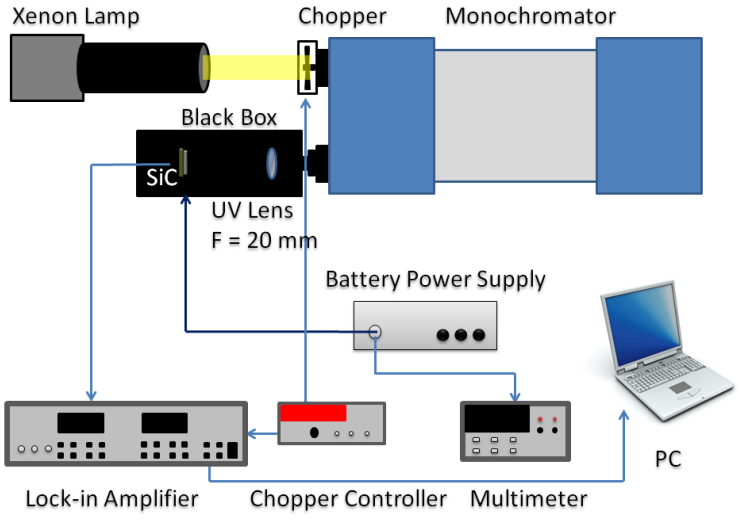

FIGURE A.7: Sketch of the experimental setup for measurements of SiC responsivity vs wavelength.

The responsivity measurements were carried out for all the above-mentioned classes of devices. In particular, in order to study the performance uniformity of electro-optical

devices, I performed a responsivity mapping in different zones of the sensitive area, at a constant voltage of 0 V and temperature of 25 °C. Such measurements proved that the devices under test show a good uniformity. At the center of the device, responsivity measurements at 3 different voltages (0 V , -3 V and -10 V) and at 4 temperatures (0 °C, 25 °C , 50 °C and 90 °C) were also performed, as shown in Fig. A.8 for the SiC8, SiC10 and SiC20 classes. Fig. A.9 shows a comparison among these responsivities as a function of the photon wavelength, at room temperature (25 °C) when a reverse bias of -10 V is applied.

In order to perform low optical power measurements, a lock-in amplifier was connected to the SiC under investigation. The incident optical power on the active area of the device was detected through a calibrated power meter and chopped at 183 Hz. I employed optical powers below 30 nW in the whole investigated wavelength range (200 - 400 nm) while the corresponding measured photocurrent values were in the 30 pA - 1.7 nA range, depending on the wavelength.

The devices performed remarkable photon detection efficiency within the range between 280 and 300 nm. The responsivity variation is due to temperature and reverse bias applied. The absolute peak was 105.1 mA/W, measured for SiC10 device at 290 nm and 0 °C.

Responsivity measurements highlight a decrease in the optical response at higher temperatures, especially at 0 V (i.e. the photodiode operating voltage for common applications). As predicted, the optical peak response at higher temperatures shifts toward slightly higher wavelengths (red shift). In contrast to the behavior of ideal devices, which actually demonstrate an increase in responsivity to higher temperatures, I have found that the responsivity values of tested devices decrease. This behavior is due to the concomitant effects of gap reduction, increase in photon lifetime and phonon contribution to the absorption of photons.

However, the above described decrease in responsivity was less pronounced, when present, at higher values of applied voltage (-3 V and -10 V) and was also established for devices with different layouts having different distances between strips in the interdigitated regions.

The observed behavior could presumably be ascribed to a decrease of the mean lifetime of the photogenerated electron-hole pairs due to the presence of non-radiative centers in the energy gap of the material. The photogenerated carriers could be captured at these centers, thus not being available for photoconduction. The existence of such effects and their dependence on voltage could be due to the effects of surface loading

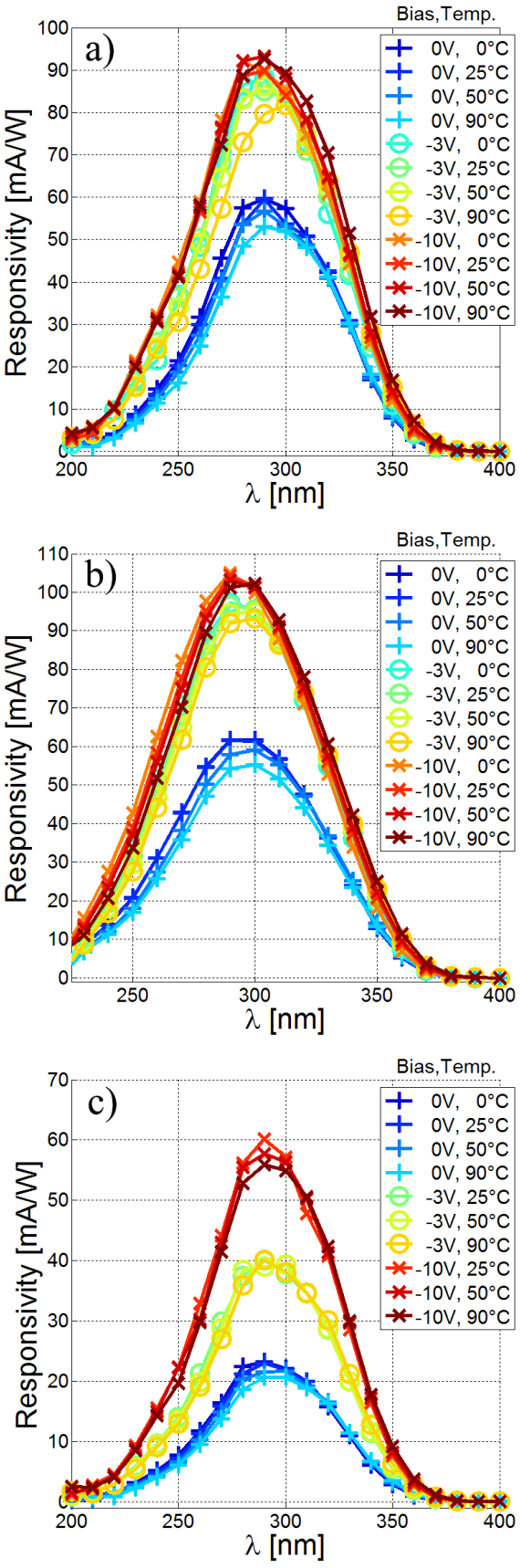

FIGURE A.8: Photoresponsivities measured at different temperatures on a typical SiC8 (a), SiC10 (b) and SiC20 (c) devices as a function of the photon wavelength for the reverse biases of 0 V, -3 V and -10 V.

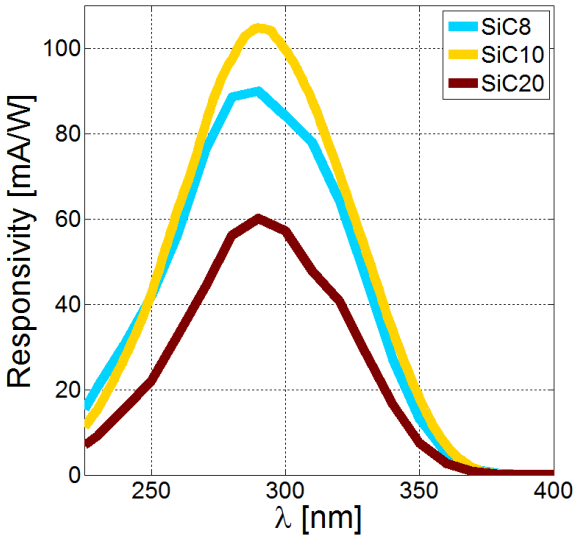

FIGURE A.9: Comparison among photoresponsivities of the SiC8, SiC10 and SiC20 as a function of the photon wavelength. The measurements were carried out at room temperature with an applied reverse bias of -10V.

induced/introduced at a certain point of the processing flow and particularly marked for devices with low-doped epitaxial layers, such as in [87].

A.4 Conclusions

In this appendix I have described the technical features of three novel classes of 4H-SiC vertical Schottky UV detectors (SiC8, SiC10, SiC20) so as to provide an electro-optical comparison based on the pinch-off surface effect also employing Ni_2Si interdigitated strips whose pitch is 8, 10 and 20 μm, respectively.

I measured, in dark conditions, forward and reverse I-V characteristics as a function of the temperature and C-V characteristics. The leakage current was a few picoamperes at -10 V and 25 °C and it increased slightly at higher temperatures, because of the very low thermal generation in the material bandgap. As expected, temperature increase produced a decrease of the bias threshold because of thermal generation. C-V characteristics show that the capacitance did not significantly decrease when the reverse bias was increased.

All three SiCs under test demonstrated a responsivity peak at 290 nm. The optical peak response at higher temperatures shifts toward slightly higher wavelengths. Also, my responsivity measurements highlight a decrease in the optical response at higher temperatures, especially at 0 V. In my experiments the SiC10 class exhibited the best

results, being the area among adjacent strips almost fully depleted (i.e. active) at -10 V, due to its increased space/strip width ratio, with respect to the SiC8. The SiC20, instead, demonstrated a lower level of performance since it does not reach full depletion.

A physical interpretation of all the results was also provided. Based on these preliminary measurements, ongoing investigations are underway so as to further improve the technical characteristics of these versatile, as well highly cost-effective, devices.

Appendix B

List of Publications

B.1 Journal papers

G. Adamo, D. Agro', S. Stivala, A. Parisi, G. C. Giaconia, A. C. Busacca, M. Mazzillo, D. Sanfilippo, and G. Fallica, *Measurements of Silicon Photomultipliers Responsivity in Continuous Wave Regime*, IEEE Transactions on Electron Devices, vol. 60, n. 11, pp. 1-8, 2013; print ISSN: 0018-9383, online ISSN: 1557-9646, DOI: 10.1109/TED.2013.2282709

R. Pernice, **G. Adamo**, S. Stivala, A. Parisi, A.C. Busacca, D. Spigolon, M. A. Sabatino, L. DAcquisto, and C. Dispenza, *Opals infiltrated with a stimuli-responsive hydrogel for ethanol vapor sensing*, Optical Materials Express, vol. 3, n. 11, pp. 1820-1833, 2013; DOI:10.1364 / OME.3.001820

B.2 International conference papers

G. Adamo, D. Agro', S. Stivala, A. Parisi, L. Curcio, A. Ando', A. Tomasino, C. Giaconia, A. C. Busacca, M. C. Mazzillo, D. Sanfilippo, and G. Fallica, *Responsivity measurements of 4H-SiC Schottky photodiodes for UV light monitoring*, Paper no. 8990-41, Photonics West 2014 - Silicon Photonics IX, Feb. 5, 2014, San Francisco, USA

G. Adamo, D. Agro', S. Stivala, A. Parisi, C. Giaconia, A. C. Busacca and G. Fallica, *SNR measurements of silicon photomultipliers in the continuous wave regime*, Paper no. 8990-43, Photonics West 2014 - Silicon Photonics IX, Feb. 5, 2014, San Francisco, USA

D. Sanfilippo, G. Valvo, M. Mazzillo, A. Piana, B. Carbone, L. Renna, P. G. Fallica, D. Agro', G. Morsellino, M. Pinto, R. Canicatti', N. Galioto, **G. Adamo**, S. Stivala, A. Parisi, L. Curcio, C. Giaconia, A. C. Busacca, R. Pagano, S. Libertino, and S. Lombardo,

Design and development of a fNIRS system prototype based on SiPM detectors, Paper no. 8990-40, Photonics West 2014 - Silicon Photonics IX, Feb. 5, 2014, San Francisco, USA

M. A. Sabatino, L. DAcquisto, G. Spadaro, S. Alessi, C. Dispenza, A. C. Busacca, R. Pernice, **G. Adamo**, S. Stivala, A. Parisi, *Photonic crystal hydrogel films responsive to ethanol vapors*, Nanoscience and Nanotechnology 2013, pp. 85 - 87, Sep. 30 - Oct. 4, 2013, Frascati

G. Adamo, D. Agro', S. Stivala, A. Parisi, C. Giaconia, A.C. Busacca, M. C. Mazzillo, D. Sanfilippo, and G. Fallica, *P-on-N and N-on-P silicon photomultipliers: responsivity comparison in the continuous wave regime*, Proc. Photonics North 2013, p. 191, Ref. number: 255-QUT5-301, Jun. 3, 2013, Ottawa, Canada

G. Adamo, D. Agro', S. Stivala, A. Parisi, C. Giaconia, A.C. Busacca, M. C. Mazzillo, D. Sanfilippo, and G. Fallica, *Responsivity measurements of N-on-P and P-on-N silicon photomultipliers in the continuous wave regime*, Proc. SPIE 8629, Photonics West 2013 - Silicon Photonics VIII, 86291, pp. 86291A-186291A-9, Mar. 14, 2013, San Francisco, USA; doi:10.1117/12.2001606

B.3 National conference papers

G. Adamo, D. Agro', S. Stivala, A. Parisi, C. Giaconia, A. Busacca, M. C. Mazzillo, D. Sanfilippo, and G. Fallica, *P-on-N and N-on-P silicon photomultipliers: an in-depth analysis in the continuous wave regime*, GE 2013, ISBN: 9788890306938, pp. 99-100, Jun. 19 - 21, 2013, Udine

D. Agro', **G. Adamo**, G. Morsellino, M. Pinto, R. Canicatti', A. Parisi, N. Galioto, A. C. Busacca, and C. Giaconia, *Design of a multichannel continuous wave fNIRS system implemented with SiPM*, GE 2013, ISBN: 9788890306938, pp. 133-134, Jun. 19 - 21, 2013, Udine

R. Pernice, **G. Adamo**, S. Stivala, A. Parisi, A. Ando', A.C. Busacca, D. Spigolon, M. A. Sabatino, L. DAcquisto, and C. Dispenza, *Ethanol vapor optical sensors based on polystyrene opals infiltrated with hydrogel*, GE 2013, ISBN: 9788890306938, pp. 113-114, Jun. 19 - 21, 2013, Udine

M. A. Sabatino, D. Spigolon, L. DAcquisto, R. Pernice, **G. Adamo**, S. Stivala, A. Parisi, A.C. Busacca, C. Dispenza, *Periodically nanostructured hydrogels for ethanol vapors sensing*, V Workshop Nazionale AICIng Tecnologie Chimiche per il Benessere e la Salute dellUomo, pp. 34-35, Jun. 13 - 14, 2013, Favignana

G. Adamo, D. Agro', S. Stivala, A. Parisi, C. Giaconia, A. Busacca, M. C. Mazzillo, D. Sanfilippo, and G. Fallica, *N-on-P and P-on-N Silicon Photomultipliers: Responsivity comparison in the continuous wave regime*, Fotonica 2013, ISBN: 9788887237160, May 21 - 23, 2013, Milano

R. Pernice, **G. Adamo**, S. Stivala, A. Parisi, A.C. Busacca, D. Spigolon, M. A. Sabatino, L. DAcquisto, and C. Dispenza, *Optical sensors for ethanol vapor based on polystyrene opals infiltrated with hydrogel*, Fotonica 2013, ISBN: 9788887237160, May 21 - 23, 2013, Milano

R. Pernice, **G. Adamo**, S. Stivala, A.C. Busacca, D. Spigolon, M. A. Sabatino, L. DAcquisto, and C. Dispenza, *Optical characterization of polystyrene direct opals and of inverse-opal hydrogels*, GE 2012, ISBN: 978-88-6741-012-5, pp. 103-104, Jun. 20 - 22, 2012, Marina di Carrara

D. Agro', **G. Adamo**, S. Stivala, A.C. Busacca, P. Livreri, M. Mazzillo, D. Sanfilippo, M. Romeo, and G. Fallica, *Measurements of silicon photomultipliers responsivity in continuous wave*, GE 2012, ISBN: 978-88-6741-012-5, pp. 87-88, Jun. 20 - 22, 2012, Marina di Carrara

G. Adamo, D. Agro', S. Stivala, A.C. Busacca, F. Principato, M. Mazzillo, D. Sanfilippo, M. Romeo, and G. Fallica, *Measurements of Silicon Photomultipliers Responsivity*, Fotonica 2012, ISBN: 9788887237146, May 15 - 17, 2012, Firenze

L. Curcio, S. Stivala, A. C. Busacca, A. Ando', **G. Adamo**, and S. Riva Sanseverino, *Second harmonic generation via random quasi-phase matching in a periodically poled lithium tantalate waveguide*, GE 2011, ISBN: 978-88-95612-85-0, pp. 117-118, Jul. 6-8, 2011, Trani

A. Ando', E. Bonanno, L. Curcio, S. Stivala, **G. Adamo**, S. Riva-Sanseverino, and A. C. Busacca, *Correlated channel model for terrestrial free space optics and project specifications evaluation of LT code in ook modulation*, GE 2011, ISBN: 978-88-95612-85-0, pp. 119-120, Jul. 6-8, 2011, Trani

A.C. Busacca, S. Stivala, L. Curcio, A. Ando', and **G. Adamo**, *Random Quasi-Phase-Matching in Tantalatio di Litio: origine del fenomeno, confronto tra propagazione bulk e guidata*, Fotonica 2011, ISBN: 9788887237122, May 9-11, 2011, Genova

Bibliography

[1] A. Einstein. Concerning an heuristic point of view toward the emission and transformation of light. *Ann. Phys.*, 17:132, 1905.

[2] V. D. Kovaltchouk, G. J. Lolos, Z. Papandreou, and K. Wolbaum. Comparison of a silicon photomultiplier to a traditional vacuum photomultiplier. *Nucl. Instrum. Methods Phys. Res. A*, 538(1):408, 2005.

[3] D. Renker. Geiger-mode avalanche photodiodes, history, properties and problems. *Nucl. Instrum. Methods Phys. Res. A*, 567(1):48, 2006.

[4] B. Dolgoshein, V. Balagura, P. Buzhan, M. Danilov, L. Filatov, E. Garutti, M. Groll, A. Ilyin, V. Kantserov, V. Kaplin, A. Karakash, F. Kayumov, S. Klemin, V. Korbel, H. Meyer, R. Mizuk, V. Morgunov, E. Novikov, P. Pakhlov, E. Popova, V. Rusinov, F. Sefkow, E. Tarkovsky, and I. Tikhomirov. Status report on silicon photomultiplier development and its applications. *Nuclear Instrum. Methods Phys. Res. A, Accel., Spectrometers, Detectors Assoc. Equip.*, 563(2):368, 2006.

[5] J. F. Cox. Fundamentals of linear electronics: integrated and discrete. *Cengage Learning*, page 91, 2004.

[6] H. Dautet, P. Deschamps, B. Dion, A. D. MacGregor, D. MacSween, R. J. McIntyre, C. Trottier, and P. P. Webb. Photon counting techniques with silicon avalanche photodiodes. *Applied Optics*, 35(12):1956, 1996.

[7] V. Golovin and V. Saveliev. Novel type of avalanche photodetector with geiger mode operation. *Nucl. Instrum. Methods Phys. Res. A*, 518(1):560, 2004.

[8] Valeri Saveliev. Silicon photomultiplier - new era of photon detection. *Advances in Optical and Photonic Devices*, page 352, 2010.

[9] F. Zappa, S. Tisa, S. Cova, P. Maccagnani, R. Saletti, R. Roncella, F. Baronti, D. Bonaccini Calia, A. Silber, G. Bonanno, and M. Belluso. Photon counting arrays for astrophysics. *J. Mod. Opt.*, 54:163–190, 2007.

[10] I. Rech, A. Gulinatti, F. Zappa, M. Ghioni, and S. Cova. High-performance silicon single-photon avalanche diode array. In *Proc. of SPIE*, pages 73200H–1–73200H–12, 2009.

[11] S. Cova, M. Ghioni, A. Lacaita, C. Samori, and F. Zappa. Avalanche photodiodes and quenching circuits for single-photon detection. *Appl. Opt.*, 35(12):1956, 1996.

[12] P. Buzhan, B. Dolgoshein, L. Filatov, A. Ilyin, V. Kantzerov, V. Kaplin, A. Karakash, F. Kayumov, S. Klemin, E. Popova, and S. Smirnov. Silicon photomultiplier and its possible applications. *Nucl. Instrum. Methods Phys. Res. A*, 518(1):560, 2003.

[13] M. Mazzillo, G. Condorelli, D. Sanfilippo, G. Valvo, B. Carbone, G. Fallica, S. Billotta, M. Belluso, G. Bonanno, L. Cosentino, A. Pappalardo, and P. Finocchiaro. Silicon photomultiplier technology at stmicroelectronics. *IEEE Trans. Nucl. Sci.*, 56(4):2434, 2009.

[14] M. Mazzillo, G. Condorelli, D. Sanfilippo, A. Piazza, G. Valvo, B. Carbone, G. Fallica, A. Pappalardo, L. Cosentino, P. Finocchiaro, M. Corselli, G. Suriani, S. Lombardo, S. Billotta, M. Belluso, and G. Bonanno. Silicon photomultipliers for nuclear medical imaging applications. *Opt. Sens., Proc. SPIE*, 7003:11, 2008.

[15] M. Mazzillo, A. Piazza, G. Condorelli, D. Sanfilippo, G. Fallica, S. Billotta, M. Belluso, G. Bonanno, L. Cosentino, A. Pappalardo, and P. Finocchiaro. Quantum detection efficiency in geiger mode avalanche photodiodes. *IEEE Trans. Nucl. Sci.*, 55(6):3620, 2008.

[16] A. G. Stewart, V. Saveliev, S. J. Bellis, D. J. Herbert, P. J. Hughes, and J. C. Jackson. Performance of $1 - mm^2$ silicon photomultiplier. *IEEE J. Quantum Electron.*, 44(2):157, 2008.

[17] S. Cova, A. Lacaita, , and G. Ripamonti. Trapping phenomena in avalanche photodiodes on nanosecond scale. *IEEE Electron Device Lett.*, 12(12):685, 1991.

[18] P. Finocchiaro, A. Pappalardo, L. Cosentino, M. Belluso, S. Billotta, G. Bonanno, B. Carbone, G. Condorelli, S. Di Mauro, G. Fallica, M. Mazzillo, A. Piazza, D. Sanfilippo, and G. Valvo. Characterization of a novel 100-channel silicon photomultiplier-part i: Noise. *IEEE Trans. Electron Devices*, 55(10):2757, 2008.

[19] P. Finocchiaro, A. Pappalardo, L. Cosentino, M. Belluso, S. Billotta, G. Bonanno, B. Carbone, G. Condorelli, S. Di Mauro, G. Fallica, M. Mazzillo, A. Piazza, D. Sanfilippo, and G. Valvo. Characterization of a novel 100-channel silicon photomultiplier-part ii: Charge and time. *IEEE Trans. Electron Devices*, 55(10): 2765, 2008.

[20] G. Barbarino, R. de Asmundis, G. De Rosa, C. M. Mollo, S. Russo, and D. Vivolo. Silicon photo multipliers detectors operating in geiger regime: An unlimited device for future applications. *Vukovar, Croatia: InTech*, 2011.

[21] M. Mazzillo, G. Condorelli, D. Sanfilippo, G. Valvo, B. Carbone, A. Piana, G. Fallica, A. Ronzhin, M. Demarteau, S. Los, and E. Ramberg. Timing performances of large area silicon photomultipliers fabricated at stmicroelectronics. *IEEE Trans. Nuclear Sci.*, 57(4):2273, 2010.

[22] A. Rochas, A. R. Pauchard, P.-A. Besse, D. Pantic, Z. Prijic, and R. S. Popovic. Low-noise silicon avalanche photodiodes fabricated in conventional cmos technologies. *IEEE Trans. Electron Devices*, 49(3):387, 2002.

[23] N. Efthimiou, G. Argyropoulos, G. Panayiotakis, M. Georgiou, and G. Loudos. Initial results on sipm performance for use in medical imaging. In *Proc. IEEE Int. Conf. IST*, July 2010.

[24] D. J. Herbert, V. Saveliev, N. Belcari, N. D'Ascenzo, A. Del Guerra, and A. Golovin. First results of scintillator readout with silicon photomultiplier. *IEEE Trans. Nuclear Sci.*, 53(1):389, 2006.

[25] P. Buzhan, B. Dolgoshein, L. Filatov, A. Ilyin, V. Kaplin, A. Karakash, S. Klemin, R. Mirzoyan, A. N. Ottec, E. Popova, V. Sosnovtsev, and M. Teshima. Large area silicon photomultipliers: Performance and applications. *Nuclear Instrum. Methods Phys. Res. A, Accel., Spectrometers, Detectors Assoc. Equip.*, 567(1):78, 2006.

[26] E. Roncali and S. R. Cherry. Application of silicon photomultipliers to positron emission tomography. In *Ann. Biomed. Eng.*, volume 39, page 1358, February 2011.

[27] N. Otte, B. Dolgoshein, and J. Hose. The sipm: A new photon detector for pet. *Nuclear Physics B, Proceedings Supplement*, 150:417, 2006.

[28] D. Contini, A. Torricelli, A. Pifferi, L. Spinelli, P. Taroni, V. Quaresima, M. Ferrari, and R. Cubeddu. Multichannel time-resolved tissue oximeter for functional imaging of the brain. *IEEE Trans. Instrum. Meas.*, 55(1):85, 2006.

[29] M. Nitzan and H. Taitelbaum. The measurement of oxygen saturation in arterial and venous blood. *IEEE Instrum. Meas. Mag.*, 11(3):9, 2008.

[30] E. Matveeva, J. Malicka, I. Gryczynski, Z. Gryczynski, and J. R. Lakowicz. Multiwavelength immunoassays using surface plasmon-coupled emission. *Biochem. Biophys. Res. Commun.*, 313(3):721, 2004.

[31] P. Eraerds, M. Legr, A. Rochas, H. Zbinden, and N. Gisin. Sipm for fast photon-counting and multiphoton detection. *Opt. Exp.*, 15(22):14539, 2007.

[32] D. Renker and E. Lorenz. Advances in solid state photon detectors. *J. Instrum.*, 4 (4):1, 2009.

[33] D. Renker. Photodetectors. *Nucl. Instrum. Meth. A*, 527:15–20, 2004.

[34] C. Piemonte. A new silicon photomultiplier structure for blue light detection. *Nucl. Instrum. Methods Phys. Res. A*, 568(1):224, 2006.

[35] F. Zappa, S. Tisa, A. Tosi, and S. Cova. Principles and features of single-photon avalanche diode arrays. *Sens. Actuators A, Phys.*, 140(1):103, 2007.

[36] G. Collazuol, G. Ambrosi, M. Boscardin, F. Corsi, G. F. Dalla Betta, A. Del Guerra, N. Dinu, M. Galimberti, D. Giulietti, L. A. Gizzi, L. Labate, G. Llosa, S. Marcatili, F. Morsani, C. Piemonte, A. Pozza, L. Zaccarelli, and N. Zorzi. Single photon timing resolution and detection efficiency of the irst silicon photo-multipliers. *Nuclear Instrum. Methods Phys. Res. A*, 581(1, 2):461, 2007.

[37] G. Adamo, D. Agro', S. Stivala, A. Parisi, G. C. Giaconia, A. C. Busacca, M. Mazzillo, D. Sanfilippo, and G. Fallica. Measurements of silicon photomultipliers responsivity in continuous wave regime. *IEEE Trans. Electron Devices*, 60(11):1, 2013.

[38] N. Dinu, K. L. Suh, R. R. Ansari, and L. Rovati. Electro-optical characterization of sipm: A comparative study. *Nuclear Instrum. Methods Phys. Res. A*, 610(1):423, 2009.

[39] D. Haensse. A new multichannel near infrared spectrophotometry system for functional studies of the brain in adults and neonates. *Opt. Exp.*, 13(12):4525, 2005.

[40] F. Zou, C. Jin, R. R. Ross, and B. Soller. Investigation of spectral interferences on the accuracy of broadband cw-nirs tissue so_2 determination. *Biomed. Opt. Exp.*, 1 (3):748, 2010.

[41] G. Salvatori, K. I. Suh, R. R. Ansari, and L. Rovati. Instrumentation and calibration protocol for a continuous wave near infrared hemoximeter. *IEEE Trans. Instrum. Meas.*, 55(4):1368, 2006.

[42] K. J. Kek, R. Kibe, M. Niwayama, N. Kudo, and K. Yamamoto. Optical imaging instrument for muscle oxygenation based on spatially resolved spectroscopy. *Opt. Exp.*, 16(22):18173, 2008.

[43] R. Pernice, G. Adamo, S. Stivala, A. Parisi, A. Busacca, D. Spigolon, M. A. Sabatino, L. D'Acquisto, and C. Dispenza. Opals infiltrated with a stimuli-responsive hydrogel for ethanol vapor sensing. *Opt. Mater. Exp.*, 3(10):18173, 2013.

[44] M. Mazzillo, A. Ronzhin, S. Los, S. Abbisso, D. Sanfilippo, G. Valvo, B. Carbone, A. Piana, G. Fallica, M. Albrow, and E. Ramberg. Electro-optical performances of p-on-n and n-on-p silicon photomultipliers. *IEEE Trans. Electron Devices*, 59(12): 3419, 2012.

[45] G. Condorelli, D. Sanfilippo, G. Valvo, M. Mazzillo, D. Bongiovanni, A. Piana, B. Carbone, and G. Fallica. Extensive electrical model of large area silicon photomultipliers. *Nucl. Instrum. Methods Phys. Res. A, Accel., Spectrometers, Detectors Assoc. Equip.*, 654(1):127, 2011.

[46] F. Corsi, C. Marzocca, A. Perrotta, A. Dragone, M. Foresta, A. Del Guerra, S. Marcatili, G. Llosa, G. Collazzuol, G.-F. Dalla Betta, N. Dinu, C. Piemonte, G. U. Pignatel, and G. Levi. Electrical characterization of silicon photo-multiplier detectors for optimal front-end design. In *Proc. IEEE Nuclear Sci. Symp. Conf. Rec.*, page 276, November 2006.

[47] H.-G. Moser, S. Hass, C. Merck, J. Ninkovic, R. Richter, G. Valceanu, N. Otte, M. Teshima, R. Mirzoyan, P. Holl, and C. Koitsch. Development of back illuminated sipm at the mpi semiconductor laboratory. In *Proc. Int. Workshop New Photon-Detectors*, page 1, June 2007.

[48] G. Adamo, D. Agro', S. Stivala, A. Parisi, C. Giaconia, A. Busacca, M. C. Mazzillo, D. Sanfilippo, and P. G. Fallica. Responsivity measurements of n-on-p and p-on-n silicon photomultipliers in the continuous wave regime. In *Proc. SPIE*, volume 8629, pages 86291A–1, March 2013.

[49] G. Adamo, D. Agro', S. Stivala, A. Parisi, C. Giaconia, A. Busacca, M. C. Mazzillo, D. Sanfilippo, and P. G. Fallica. P-on-n and n-on-p silicon photomultipliers: responsivity comparison in the continuous wave regime. In *Proc. Photonics North 2013*, page 191, June 2013.

[50] T. Achtnich and F. Braun. Design and evaluation of a modular fnirs probe for employment in neuroimaging applications. *Eidgenossische Technische Hochschule Zurich, Institut fur Biomedizinische Technik*, 2012. URL http://dx.doi.org/10.3929/ethz-a-007564212.

[51] Hamamatsu Photonics K.K. Photon counting using photomultiplier tubes. 1998. URL http://mccombe.physics.buffalo.edu/lab-manuals/photoncounting.pdf.

[52] Sensl. Noise in silicon photomultipliers and vacuum photomultiplier tubes. 2008. URL http://www.photonicsonline.com/doc/noise-in-silicon-photomultipliers-and-vacuum-0003.

[53] P. Jiang, J. F. Bertone, K. S. Hwang, and V. L. Colvin. Single-crystal colloidal multilayers of controlled thickness. *Chem. Mater.*, 11(8):2132, 1999.

[54] M. A. Sabatino, L. D'Acquisto, G. Spadaro, S. Alessi, C. Dispenza, A.C. Busacca, R. Pernice, G. Adamo, S. Stivala, and A. Parisi. Photonic crystal hydrogel films responsive to ethanol vapors. In *Proceedings of Nanoscience and Nanotechnology 2013*, pages 85–87, 2013.

[55] E. Pavarini, L. C. Andreani, C. Soci, M. Galli, F. Marabelli, and D. Comoretto. Band structure and optical properties of opal photonic crystals. *Phys. Rev. B*, 72 (4), 2005.

[56] M. Allard, E. H. Sargent, E. Kumacheva, and O. Kalinina. Characterization of internal order of colloidal crystals by optical diffraction. *Opt. Quantum Electron*, 34(1-3):27, 2002.

[57] L. Y. Yang and W. B. Liau. Optical responses of polyaniline inverse opals to chemicals. *Synth. Met.*, 160(17-18):1809, 2010.

[58] S. Achelle, Á. Blanco, M. López-García, R. Sapienza, M. Ibisate, C. López, and J. Rodríguez-López. Newpoly(phenylene-vinylene)-methyl methacrylate-based photonic crystals. *J. Polym. Sci. A Polym. Chem.*, 48(12):2659, 2010.

[59] S. N. Kasarova, N. G. Sultanova, C. D. Ivanov, and I. D. Nikolov. Analysis of the dispersion of optical plastic materials. *Opt. Mater.*, 29(11):1481, 2007.

[60] S. M. Abrarov, T. W. Kim, and T. W. Kang. Equations for filling factor estimation in opal matrix: Addendum to [opt. commun. 259, 383 (2006)]. *Opt. Commun.*, 264 (1):240, 2006.

[61] V. Morandi, F. Marabelli, V. Amendola, M. Meneghetti, and D. Comoretto. Colloidal photonic crystals doped with gold nanoparticles: spectroscopy and optical switching properties. *Adv. Funct. Mater.*, 17(15):2779, 2007.

[62] D. M. Mittleman, J. F. Bertone, P. Jiang, K. S. Hwang, and V. L. Colvin. Optical properties of planar colloidal crystals: Dynamical diffraction and the scalar wave approximation. *J. Chem. Phys.*, 111(1):345, 1999.

[63] J. Vetelino and A. Reghu. Introduction to sensors. 2012.

[64] G. Eranna, R. Paris, and T. Doll. Sensor response time evaluations of trace hydrogen gaseous species with platinum using kelvin probe. In *Proceedings of IEEE Sensors 2012*, pages 1–4, 2012.

[65] J. Y. Wang, Y. Cao, Y. Feng, F. Yin, and J. P. Gao. Multiresponsive inverse-opal hydrogels. *Adv. Mater.*, 19(22):3865, 2007.

[66] J. Yan M. Zhou Z. Pan, J. Ma and J. Gao. Response of inverse-opal hydrogels to alcohols. *J. Mater. Chem.*, 22(5):2018, 2012.

[67] A. D'Amico and C. Di Natale. A contribution on some basic definitions of sensors properties. *IEEE Sens. J.*, 1(3):183, 2001.

[68] R. St-Gelais, G. Mackey, J. Saunders, J. Zhou, A. Leblanc-Hotte, A. Poulin, J. A. Barnes, H.-P. Loock, R. S. Brown, and Y.-A. Peter. A fabry-perot refractometer for chemical vapor sensing by solid-phase microextraction. In *Proceedings of IEEE/LEOS International Conference on Optical MEMS and Nanophotonics*, pages 85–86, 2011.

[69] R. St-Gelais, G. Mackey, J. Saunders, J. Zhou, A. Leblanc-Hotte, A. Poulin, J. A. Barnes, H.-P. Loock, R. S. Brown, and Y.-A. Peter. Gas sensing using polymer-functionalized deformable fabry-perot interferometers. *Sens. Actuators B Chem.*, 182(3):45, 2013.

[70] A. Bearzotti, A. Macagnano, S. Pantalei, E. Zampetti, I. Venditti, I. Fratoddi, and M. V. Russo. Alcohol vapor sensory properties of nanostructured conjugated polymers. *J. Phys. Condens. Matter*, 20(47):474207, 2008.

[71] S. Li, D. Hu, J. Huang, and L. Cai. Optical sensing nanostructures for porous silicon rugate filters. *Nanoscale Res. Lett.*, 7(1):79, 2012.

[72] X. Xu, A. V. Goponenko, and S. A. Asher. Polymerized polyhema photonic crystals: ph and ethanol sensor materials. *J. Am. Chem. Soc.*, 130(10):3113, 2008.

[73] C. Chen, Y. Zhu, H. Bao, J. Shen, H. Jiang, L. Peng, X. Yang, C. Li, and G. Chen. Ethanol-assisted multisensitive poly(vinyl alcohol) photonic crystal sensor. *Chem. Commun. (Camb.)*, 47(19):5530, 2011.

[74] M. Razeghi and A. Rogalski. Semiconductor ultraviolet detectors. *J. Appl. Phys.*, 79(10):7433, 1996.

[75] M. Mazzillo, A. Sciuto, F. Roccaforte, and V. Raineri. 4h-sic schottky photodiodes for ultraviolet light detection. In *IEEE Nucl. Sci. Symp. Conf. Rec.*, pages 1642–1646, 2011.

[76] E. Monroy, F. Omnes, and F. Calle. Wide-bandgap semiconductor ultraviolet photodetectors. *Semicond. Sci. Technol.*, 18(4):R33, 2003.

[77] G. A. Shaw, A. M. Siegel, J. Model, A. Geboff, S. Soloviev, A. Vert, and P. Sandvik. Deep-uv photon counting detectors and applications. In *Proc. SPIE 7320*, 2009.

[78] P. Schreiber, T. Dang, T. Pickenpaugh, G. Smith, P. Gehred, and C. Litton. Solar blind uv region and uv detector development objectives. In *Proc. SPIE 3629 Int. Soc. Opt. Eng.*, page 230248, 1999.

[79] D. Engelhaupt, P. Reardon, L. Blackwell, L. Warden, and B. Ramsey. Autonomous long-range open area fire detection and reporting. In *Proc. SPIE 5782 Int. Soc. Opt. Eng.*, pages 164–175, 2005.

[80] A. Vert, S. Soloviev, J. Fronheiser, and P. Sandvik. Solar-blind 4h-sic single-photon avalanche diode operating in geiger mode. *IEEE Photon. Technol. Lett.*, 20(18): 1587, 2008.

[81] S. Metzger, H. Henschel, O. Kohn, and W. Lennartz. Silicon carbide radiation detector for harsh environments. *IEEE Trans. Nucl. Sci.*, 49(3):1351, 2002.

[82] M. Holz, G. Hultsch, T. Scherg, and R. Rupp. Reliability considerations for recent infineon sic diode releases. *Microelectron. Reliab.*, 47(9-11):1741, 2007.

[83] M. A. Borysiewicz, E. Kaminska, M. Mysliwiec, M. Wzorek, A. Kuchuk, A. Barcz, E. Dynowska, M. A. Di Forte-Poisson, C. Giesen, and A. Piotrowska. Fundamentals and practice of metal contacts to wide band gap semiconductor devices. *Cryst. Res. Technol.*, 47(3):261, 2012.

[84] B. K. Ng, F. Yan, J. P. R. David, R. C. Tozer, G. J. Rees, C. Qin, and J. H. Zhao. Multiplication and excess noise characteristics of thin 4h-sic uv avalanche photodiodes. *IEEE Photon. Technol. Lett.*, 14(9):1342, 2002.

[85] A. Sciuto, F. Roccaforte, S. Di Franco, and V. Raineri. High responsivity 4h-sic schottky uv photodiodes based on the pinch-off surface effect. *Appl. Phys. Lett.*, 89 (8):081111, 2006.

[86] A. Sciuto, M. Mazzillo, V. Raineri, G. Catania, G. D'Arrigo, and F. Roccaforte. On the aging effects of 4h-sic schottky photodiodes under high intensity mercury lamp irradiation. *IEEE Photonics Technol. Lett.*, 22(11):775, 2010.

[87] G. Adamo, D. Agro', S. Stivala, A. Parisi, L. Curcio, A. Ando', A. Tomasino, C. Giaconia, A. Busacca, M. C. Mazzillo, D. Sanfilippo, and P. G. Fallica. Responsivity measurements of 4h-sic schottky photodiodes for uv light monitoring. In *Proc. SPIE*, volume 8990, March 2014.